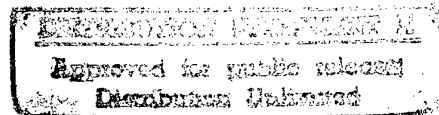




UNIVERSITY COLLEGE LONDON

Department of Electronic and Electrical Engineering



Wideband Modulation and Tuning of Semiconductor Lasers using Novel Quantum well Structures

Contract F61708-94-C0009

Final Report

DTIC QUALITY INSPECTED 8

prepared by

Xuan Huang and Alwyn Seeds

July, 1996

TORRINGTON PLACE LONDON WC1E 7JE UK

Telephone: +44 171-380 7928

Facsimile: +44 171-387 4350

19961113 143

REPORT DOCUMENTATION PAGE

Form Approved OMB No. 0704-0188

Public reporting burden for this collection of information is estimated to average 1 hour per response, including the time for reviewing instructions, searching existing data sources, gathering and maintaining the data needed, and completing and reviewing the collection of information. Send comments regarding this burden estimate or any other aspect of this collection of information, including suggestions for reducing this burden to Washington Headquarters Services, Directorate for Information Operations and Reports, 1215 Jefferson Davis Highway, Suite 1204, Arlington, VA 22202-4302, and to the Office of Management and Budget, Paperwork Reduction Project (0704-0188), Washington, DC 20503.

1. AGENCY USE ONLY (Leave blank)		2. REPORT DATE July 1996	3. REPORT TYPE AND DATES COVERED Final	
4. TITLE AND SUBTITLE Wideband Modulation and Tuning of Semiconductor Lasers Using Novel Quantum Well Structures			5. FUNDING NUMBERS F61708-94-C0009 or SPC94-4035	
6. AUTHOR(S) Xuan Huang and Alwyn Seeds				
7. PERFORMING ORGANIZATION NAME(S) AND ADDRESS(ES) University College London Department of Electronic and Electrical Engineering Torrington Place London WC1E 7JE			8. PERFORMING ORGANIZATION REPORT NUMBER SPC94-4035	
9. SPONSORING/MONITORING AGENCY NAME(S) AND ADDRESS(ES) EOARD PSC 802 BOX 14 FPO AE 09499-0200			10. SPONSORING/MONITORING AGENCY REPORT NUMBER SPC94-4035	
11. SUPPLEMENTARY NOTES				
12a. DISTRIBUTION/AVAILABILITY STATEMENT Unlimited			12b. DISTRIBUTION CODE	
13. ABSTRACT (Maximum 200 words) Angle modulation techniques enable analogue optical transmission systems to be realised which have dynamic ranges in excess of those possible with conventional intensity modulation direct detection (IMDD) links. Tunable semiconductor lasers are essential components for links employing optical frequency modulation (OFM) for enhanced dynamic range or dense wavelength division multiplex (DWDM) for multi-channel capability. They are also key components in many advanced sensor systems. Existing lasers use the forward bias injection effect (CIE) to obtain tuning. Whilst this is a convenient technique for wavelength setting it suffers from severe limitations when fast tuning or modulation. Of the laser frequency is required. At low modulation frequencies the response is dominated by thermal effects, leading to a decrease in emission frequency with increasing current, whereas at high frequencies the response is dominated by plasma and band filling effects giving an increase in frequency with increasing current. The resulting overall frequency response typically varies by more than an order of magnitude 0-1 Ghz accompanies by phase variations of up to π radians. Equalising such a response even over a restricted frequency range, requires complex networks that have to be optimised for the particular laser and its operating conditions. Improved uniformity of response has been obtained in multi-electrode distributed feedback (DFB) lasers by critical adjustment of the distribution of current between sections, but the settings needed are highly sample dependent, and may drift with laser ageing, making this an unreliable approach.				
14. SUBJECT TERMS			15. NUMBER OF PAGES 73	
			16. PRICE CODE	
17. SECURITY CLASSIFICATION OF REPORT UNCLASSIFIED	18. SECURITY CLASSIFICATION OF THIS PAGE UNCLASSIFIED	19. SECURITY CLASSIFICATION OF ABSTRACT UNCLASSIFIED	20. LIMITATION OF ABSTRACT UL	

NSN 7540-01-280-5500

Standard Form 298 (Rev. 2-89)
Prescribed by ANSI Std. Z39-18
298-102

Contents

Abstract	2
Introduction.....	3
Chapter 1. Device Modelling and Calculation	4
1.1 Modelling of optical field profile in a ridge waveguide	5
1.2. The calculation of optical confinement factor	19
1.3. The calculation of absorption spectrum and refractive index from experimental transmission spectra.....	27
1.4. Calculations relating to tuning performance	31
Chapter 2. Device Fabrication Progress	38
2.1. Ohmic contact on p-GaAs improvement	39
2.2 Chemical wet etch in defining ridge	41
2.3 Improvements in laser die bonding	44
2.4. Ion implantation processing	45
2.4.1. O+ implantation	45
2.4.2 H+ implantation	47
2.5. Band gap shifting processing	49
Chapter 3. Device Tuning Performance	53
3.1. General device characteristics	53
3.2. Static tuning performance	54
3.2.1. Optical power output during tuning	54
3.2.2. Tuning performance	59
3.3. Dynamic tuning	60
Chapter 4 Work in Progress and Future work	70
Chapter 5 Conclusion	73

Abstract

Angle modulation techniques enable analogue optical transmission systems to be realised which have dynamic ranges in excess of those possible with conventional intensity modulation direct detection (IMDD) links. Tunable semiconductor lasers are essential components for links employing optical frequency modulation (OFM) for enhanced dynamic range or dense wavelength division multiplex (DWDM) for multi-channel capability. They are also key components in many advanced sensor systems. Existing lasers use the forward bias carrier injection effect (CIE) to achieve tuning. Whilst this is a convenient technique for wavelength setting it suffers from severe limitations when fast tuning or modulation of the laser frequency is required. At low modulation frequencies the response is dominated by thermal effects, leading to a decrease in emission frequency with increasing current, whereas at high frequencies the response is dominated by plasma and band filling effects giving an increase in frequency with increasing current. The resulting overall frequency response typically varies by more than an order of magnitude from 0-1GHz accompanied by phase variations of up to π radians. Equalising such a response, even over a restricted frequency range, requires complex networks that have to be optimised for the particular laser and its operating conditions. Improved uniformity of response has been obtained in multi-electrode distributed feedback (DFB) lasers by critical adjustment of the distribution of current between sections, but the settings needed are highly sample dependent, and may drift with laser ageing, making this an unreliable approach

We previously demonstrated, for the first time, a novel external cavity semiconductor laser tuning technique using the refractive index change in reverse biased multiple quantum well (MQW) PIN structures. The technique yielded a tuning response that was uniform to within ± 1.6 dB from 30 kHz to 1.3 GHz, the upper frequency limit being set by the parasitic capacitance of the tuning element. The objective of this programme is to apply the same technique in a monolithically integrated tunable laser. In the first year of the programme, funded under special contract SPC-93-4072, we designed and fabricated successfully a two section ridge guide laser to explore the tuning technique. In this second year of the programme we have developed and demonstrated inter-section isolation and quantum well disordering techniques, leading to the successful fabrication of a monolithically integrated reverse bias tuned quantum well laser having FM response uniform to within ± 2.5 dB from 5 kHz to 500 MHz and ± 0.75 dB from 10 kHz to 100 MHz. We report in detail on the fabrication and assessment techniques and the results obtained.

Introduction

In our first year report, we introduced the purpose of this project, reviewed existing approaches to tunable lasers, presented different tuning configurations from external cavity tuning to integrated monolithic tuning, and discussed different tuning mechanisms including the electro-optic effect, the acoust-optic effect, the carrier injection effect (CIE) and the quantum confined Stark effect (QCSE) in a MQW structure. We decided to use QCSE as the tuning mechanism and described the design of a 2-section integrated Fabry-Perot cavity ridge waveguide tunable laser, to demonstrate fast tuning and flat modulation response. Device fabrication techniques were described, and preliminary experimental results, mainly the successful realisation of a CW laser and its characterisation, were presented.

During the second year, progress has been achieved in the following aspects. Modelling and calculation have been performed on the field profile in the waveguide, optical confinement factor, tuning performance and absorption - refractive index conversion. Fabrication techniques have been developed to reduce contact resistance, improve the die soldering technique using eutectic alloy instead of indium, and improve the trench etching technique to give uniform ridge dimensions. These developments gave improved power output and single mode performance. Ion implantation by H^+ and O^+ was carried out over a range of different doses and energies. H^+ implantation gave well isolated two section tunable lasers. Experiments on impurity free vacancy diffusion (IFVD) by SiO_2 and SrF_2 cap annealing were performed, leading to 12nm laser emission wavelength shift. A new IFVD technique for better device performance is suggested. Due to the success in device fabrication, static and dynamic tuning performance has been evaluated, giving tuning exceeding the Fabry-Perot mode space and highly uniform FM response. The experimental results are analysed in great detail to reveal the mechanisms involved and the route to further performance enhancement.

The report is organised as follows. Chapter 1 describes device modelling and calculation; Chapter 2, device fabrication progress; Chapter 3, device tuning performance; Chapter 4, work in process and future work and Chapter 5, conclusion.

Chapter 1. Device Modelling and Calculation

As described in our first year report, the integrated tunable laser is a 2-section Fabry-Perot cavity, metal clad ridge waveguide laser, as shown in Fig.1.1 .

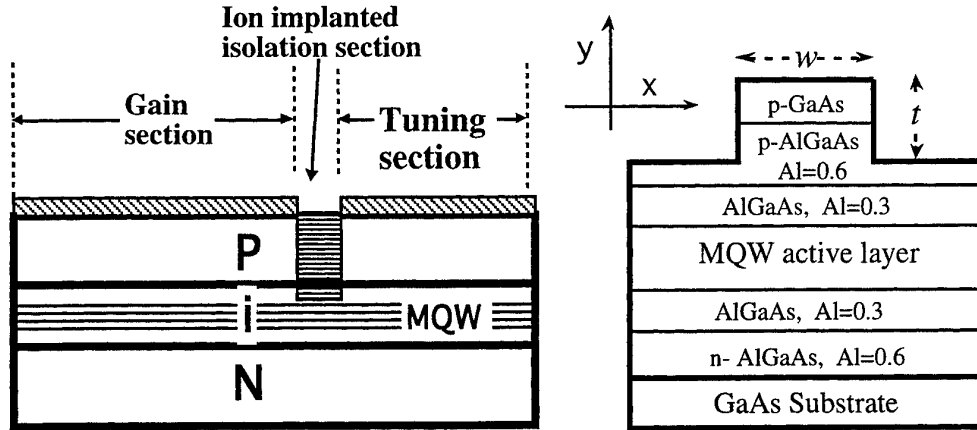


Fig. 1.1. 2-section ridge waveguide tunable laser schematic structure.

The rib width w and the rib height t , are the most important parameters in deciding the laser mode behaviours. This is because the ridge waveguide is a weakly index guided waveguide structure. The lateral mode is defined by the ridge width and the effective refractive index difference on the two side walls, reducing t will provide larger effective index difference and better lateral mode confinement, but will result in increased field leakage. Therefore, to model the field profile in a chosen structure is very important in deciding correct value for w and t in order to achieve good lateral mode performance. This will be dealt with in section 1.1.

The tuning is achieved by QCSE which induces refractive index change. This only happens within the volume of the MQW structure. The index change will influence the whole guided field in a way that depends on how much field energy is confined within this MQW volume, that is the confinement factor Γ . The calculation of confinement factor will be discussed in section 1.2 .

For an MQW structure wafer, direct measurement of the refractive index variation with applied external electrical field is very difficult, but measuring the transmission spectrum is relatively straight forward. The procedure to convert experimental transmission spectra into absorption spectra and hence calculate the refractive index change is introduced in section 1.3 .

Knowing the confinement factor and refractive index change, the tuning performance can be predicted, such as the optimum length of the tuning section, and structural parameters can be determined. The procedure for this is discussed in section 1.4.

1.1 Modelling of optical field profile in a ridge waveguide

Since the description of all optical phenomena is mathematically based on Maxwell's equations, it is appropriate to start the discussion of semiconductor laser by considering these equations in some detail. In MKS system, Maxwell's equations take the form¹:

$$\nabla \times \mathcal{E} = -\partial \mathcal{B} / \partial t \quad (1.1)$$

$$\nabla \times \mathcal{H} = \mathcal{J} + \partial \mathcal{D} / \partial t \quad (1.2)$$

$$\nabla \cdot \mathcal{D} = \rho_f \quad (1.3)$$

$$\nabla \cdot \mathcal{B} = 0 \quad (1.4)$$

where \mathcal{E} and \mathcal{H} are the electric and magnetic field vectors, and \mathcal{D} and \mathcal{B} are the corresponding electric and magnetic flux densities. The current density vector \mathcal{J} and the charge density ρ_f represent the sources for the electromagnetic field. The flux densities \mathcal{D} and \mathcal{B} arise in response to the electric and magnetic field \mathcal{E} and \mathcal{H} propagating inside the medium, and their relationship depends on details of the matter-radiation interaction. For a nonmagnetic dielectric medium the relationship can be expressed as the constitutive relations:

$$\mathcal{D} = \epsilon_0 \mathcal{E} + \mathcal{P} \quad (1.5)$$

$$\mathcal{B} = \mu_0 \mathcal{H} \quad (1.6)$$

$$\mathcal{J} = \sigma \mathcal{E} \quad (1.7)$$

where ϵ_0 is the vacuum permittivity, μ_0 is the vacuum permeability, and σ is the conductivity of the medium. The induced electric polarisation \mathcal{P} is calculated quantum mechanically. For a semiconductor material, its evaluation requires the knowledge of the Bloch wave functions and the density of states for the conduction and valence bands. In order to describe the propagation of an optical field inside the medium, we take curl of (1.1) to get

$$\nabla \times \nabla \times \mathcal{E} = -\mu_0 \frac{\partial}{\partial t} (\nabla \times \mathcal{H}) \quad (1.8)$$

where Eq.(1.6) has been used. With the help of Eqs. (1.2), (1.5) and (1.7), we can eliminate \mathcal{H} , \mathcal{J} and \mathcal{D} in favor of \mathcal{E} and \mathcal{P} to obtain

$$\nabla \times \nabla \times \mathcal{E} = -\mu_0 \sigma \frac{\partial \mathcal{E}}{\partial t} - \mu_0 \epsilon_0 \frac{\partial^2 \mathcal{E}}{\partial t^2} - \mu_0 \frac{\partial^2 \mathcal{P}}{\partial t^2} \quad (1.9)$$

The left hand side can be simplified by

$$\nabla \times \nabla \times \mathcal{E} = \nabla (\nabla \cdot \mathcal{E}) - \nabla^2 \mathcal{E} \quad (1.10)$$

In the absence of free charges, $\rho_f = 0$, and from (1.3) and (1.5), we obtain

$$\nabla \cdot \mathcal{D} = \epsilon_0 \nabla \cdot \mathcal{E} + \nabla \cdot \mathcal{P} = 0 \quad (1.11)$$

The term $\nabla \cdot \mathcal{P}$ is negligible in most case of practical interest and, consequently, $\nabla \cdot \mathcal{E} = 0$ in (1.10). Equation (1.9) then becomes

$$\nabla^2 \mathcal{E} - \frac{\sigma}{\epsilon_0 c^2} \frac{\partial \mathcal{E}}{\partial t} - \frac{1}{c^2} \frac{\partial^2 \mathcal{E}}{\partial t^2} = \frac{1}{\epsilon_0 c^2} \frac{\partial^2 \mathcal{P}}{\partial t^2} \quad (1.12)$$

where we have used the relation

$$\mu_0 \epsilon_0 = \frac{1}{c^2} \quad (1.13)$$

and c is the speed of light in vacuum. The wave equation (1.12) is valid for arbitrary time-varying fields. In an optical field with harmonic time variations, the field can be decomposed into its sinusoidal Fourier components. Using the complex notation, we have

$$\mathcal{E}(x, y, z, t) = \text{Re}[\mathbf{E}(x, y, z) \exp(-i\omega t)] \quad (1.14)$$

$$\mathcal{P}(x, y, z, t) = \text{Re}[\mathbf{P}(x, y, z) \exp(-i\omega t)] \quad (1.15)$$

where $\omega = 2\pi\nu$ is the angular frequency and $\nu = c/\lambda$ is the optical field oscillation frequency at the vacuum wavelength λ . Note \mathbf{E} and \mathbf{P} are generally complex as they contain the phase information. Using (1.14) and (1.15) in (1.12), we obtain

$$\nabla^2 \mathbf{E} + \kappa_0^2 \left[1 + \frac{i\sigma}{\epsilon_0 \omega} \right] \mathbf{E} = -\frac{\kappa_0^2}{\epsilon_0} \mathbf{P} \quad (1.16)$$

where $\kappa_0 = \omega/c = 2\pi/\lambda$ is the vacuum wave number. Under steady state conditions the response of the medium to the electric field is governed by the susceptibility χ defined by

$$\mathbf{P} = \epsilon_0 \chi(\omega) \mathbf{E} \quad (1.17)$$

where χ is dependent on frequency due to the dispersive nature of the medium response. In general χ is a second-rank tensor. For an isotropic medium, χ is a scalar. It is useful to decompose χ into two parts

$$\chi = \chi_o + \chi_p \quad (1.18)$$

where χ_o is the medium susceptibility in the absence of external pumping and χ_p is the additional contribution to the susceptibility related to the strength of pumping. In the case of semiconductor lasers, current injection is the source of pumping and χ_p depends on the concentration of charge carriers in the active layer. Both χ_o and χ_p are generally complex and frequency-dependent. Using (1.17) in (1.16), we finally obtain the time-independent wave equation

$$\nabla^2 \mathbf{E} + \epsilon \kappa_0^2 \mathbf{E} = 0 \quad (1.19)$$

where we introduced the complex dielectric constant

$$\epsilon = \epsilon' + i\epsilon'' = \epsilon_b + i\text{Im}(\chi_o) + \chi_p + i\sigma/(\epsilon_0 \omega) \quad (1.20)$$

and $\epsilon_b = 1 + \text{Re}(\chi_o)$ is the background dielectric constant of unpumped material and is real. The wave equation (1.19) is the basic equation used to obtain the spatial mode structure of the optical field. Mathematically, a laser mode is the specific solution of

this equation that satisfies all the boundary conditions imposed by the laser structure. In general multimode case, the optical field is denoted by E_{pqm} , where m, an integer denotes the longitudinal modes, and p, q also integers, stand for the lateral and transverse modes specifying the field distribution in the direction parallel and perpendicular to the junction plane, respectively. Since it is often desirable to design lasers emitting light predominantly in a single mode, to calculate or model the allowed mode number and its field distribution is essential for the lasers control.

In heterostructure semiconductor lasers the field confinement in the transverse direction (normal to the junction plane) occurs through dielectric waveguiding,^{2,3} that is index guiding since the refractive index discontinuity between the active and cladding layers is responsible for the mode confinement through the total internal reflection occurring at the interface. However, field confinement in the lateral direction (parallel to the junction plane) is not always due to index guiding. Depending on the lateral field mode confinement details, semiconductor lasers can be classified as gain-guided in which the mode is confined by the lateral variation of optical gain or index-guided in which the lateral variation of refractive index confines the mode. A stripe geometry laser is a typical gain-guided laser.⁴ Index-guided lasers can be further subclassified as weakly or strongly index-guided depending on the magnitude of the lateral index step. Buried rib waveguide laser⁵, often used in the InP long wavelength laser material system, is an example of a strongly index-guided laser while the metal clad ridge waveguide laser⁶, which is often used in GaAs material system, is a weakly index-guided laser as the index step is achieved by the effective refractive index difference between the ridge centre and the edge region.

To further describe the laser mode, the dielectric constant ϵ in (1.19) can be assumed to vary with x, y, but be independent of z, where x is parallel, y is normal to the heterojunction, while z is along the cavity as shown in Fig.1.1 . The time independent wave equation is then

$$\nabla^2 \mathbf{E} + \epsilon(x, y) \kappa_0^2 \mathbf{E} = 0 \quad (1.21)$$

$$\text{and } \epsilon(x, y) = \epsilon_j(x) \quad (1.22)$$

where the subscript j numbers various layers in the heterostructure laser. To account for absorption, ϵ_j is complex in each layer, and also varies with external pumping as shown by (1.20). Often the dielectric constant $\epsilon(x, y)$ varies slowly in the lateral x direction compared to its variation in the transverse y direction. To a good approximation, the slab waveguide problem in the y direction can be solved for each x and the resulting solution can then be used to account for the lateral variation. Therefore,

$$\epsilon(x,y) \mathbf{E} \equiv \bar{\mathbf{e}}\phi(y;x)\Psi(x)\exp(i\beta z) \quad (1.23)$$

where β is the propagation constant and $\bar{\mathbf{e}}$ is the unit vector of the electric field. On substituting (1.23) into (1.21):

$$\frac{1}{\Psi} \frac{\partial^2 \Psi}{\partial x^2} + \frac{1}{\phi} \frac{\partial^2 \phi}{\partial y^2} + [\epsilon(x,y)\kappa_0^2 - \beta^2] = 0 \quad (1.24)$$

In the effective index approximation, the transverse field distribution $\phi(y;x)$ is obtained first by solving

$$\frac{\partial^2 \phi}{\partial y^2} + [\epsilon(x,y)\kappa_0^2 - \beta_{eff}^2(x)] = 0 \quad (1.25)$$

where β_{eff} is the effective propagation constant for a fixed value of x . The lateral field distribution is then obtained by solving

$$\frac{\partial^2 \Psi}{\partial x^2} + [\beta_{eff}^2(x) - \beta^2] = 0 \quad (1.26)$$

For a given laser structure, (1.25) and (1.26) can be used to obtain the transverse and lateral modes, respectively. Since $\epsilon(x,y)$ is generally complex, β_{eff} is also complex.

The effective index of refraction is defined as

$$n_{eff}(x) = \beta_{eff}(x) / \kappa_0 \quad (1.27)$$

and is itself complex.

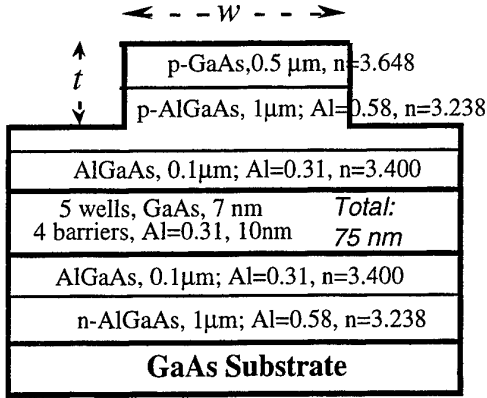
To obtain an exact solution of (1.25) and (1.26) is a difficult task. By using the effective index method⁷ and the finite difference modelling⁸, one can solve numerically the field equation by inputting the laser structure and boundary condition information. A software, called FWave III based on this model has been developed by Dr M. Taylor in The University of Glasgow. The program solves explicitly the horizontal and vertical components of the electric field, and calculates the effective index of the waveguide corresponding to each mode.

By using FWave, a number of heterostructures with different ridge width w and height t are modelled. During the modelling, the average refractive index in the MQW region is calculated by the weighted geometric average method⁹, which is proved to be good enough in representing the effect of MQW structure on the refractive index of this region.¹⁰ The expression is

$$\bar{n} = \sqrt{\frac{\sum_{i=1}^{i=m} d_i n_i^2}{\sum_{i=1}^{i=m} d_i}} \quad (1.28)$$

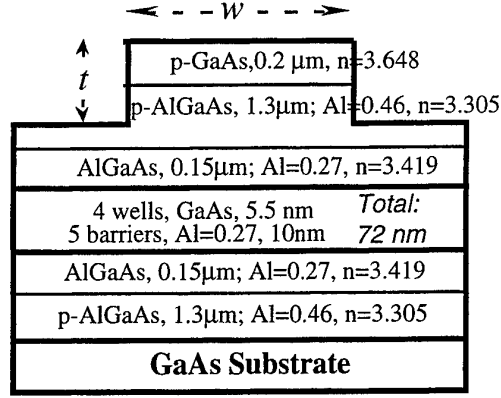
where \bar{n} is the average refractive index in the MQW, and d_i, n_i are respectively the thickness and refractive index of each layer comprising the MQW. The refractive index corresponding to each layer with different Al composition is calculated based

on published data^{11,12} by interpolating techniques. Four structures, which are the samples grown by Sheffield, have been modelled. The heterostructures, together with refractive index for each layer, are shown in Fig.1.2.



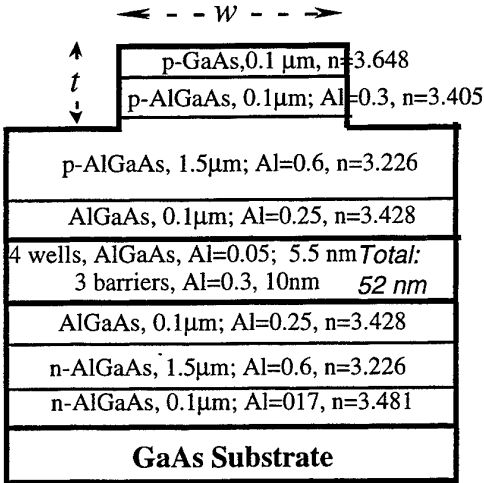
MQW active layer: $\bar{n} = 3.518$

QT703R



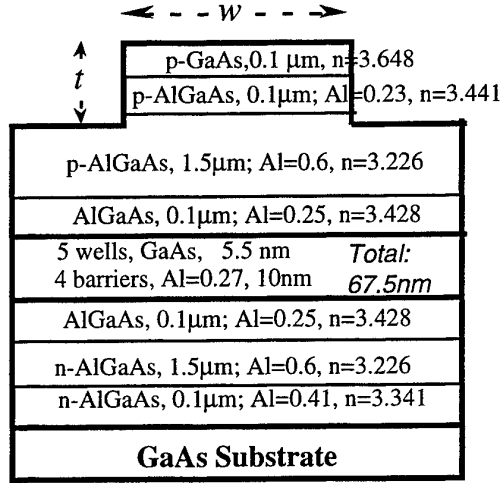
MQW active layer: $\bar{n} = 3.491$

QT787



MQW active layer: $\bar{n} = 3.513$

QT862



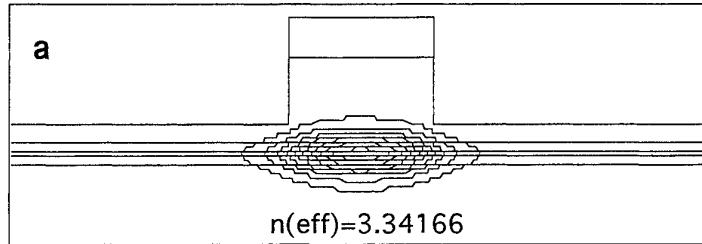
MQW active layer: $\bar{n} = 3.514$

QT863

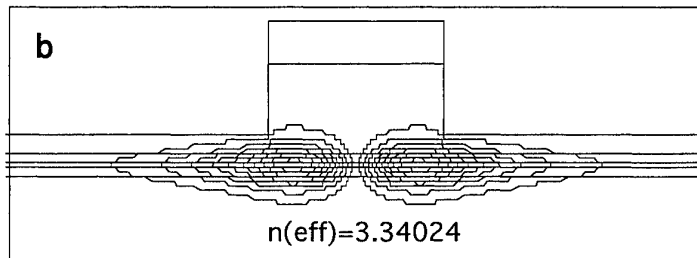
Fig. 1.2. Four epitaxial heterostructures for field modelling. Corresponding layer refractive index is denoted.

The modelling results shown in Fig.1.3. to Fig.1.6 are for the QT703R heterostructure with different ridge widths w and heights t . In Fig.1.3., with $w=5 \mu\text{m}$ and $t=1.3 \mu\text{m}$, the results show the waveguide supports TE_{00} and possibly, TE_{10} as well because in a laser, whether a mode is supported or not depends firstly, the mode should be on the

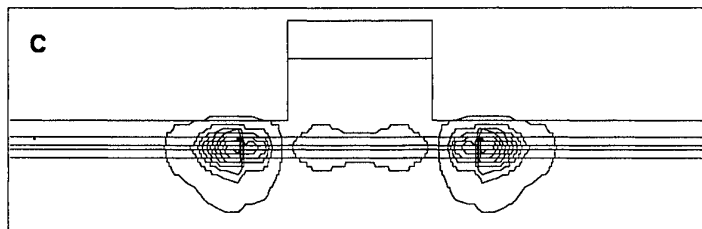
$w=5, t=1.3 \mu\text{m}$; TE₀₀; 10% contour step



$w=5, t=1.3 \mu\text{m}$; TE₁₀; 10% contour step



$w=5, t=1.3 \mu\text{m}$; TE₂₀; 10% contour step, but the most out one=1%.



$w=5, t=1.3 \mu\text{m}$; TE₃₀; 10% contour step

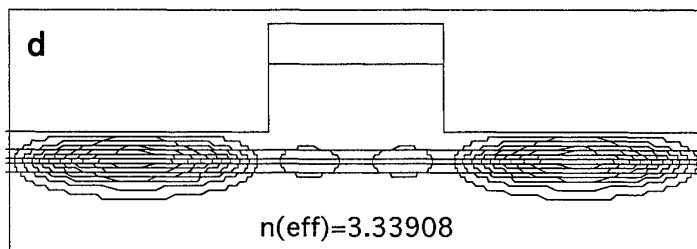


Fig.1.3. Field modelling results for QT703R with $w=5\mu\text{m}$, $t=1.3 \mu\text{m}$.

overlap with the gain region as more as possible, or in other words, the mode confinement factor (the ratio of optical energy within a certain mode divided by total optical energy) should as high as possible, and secondly, the mode should be supported by the waveguide. With the ridge waveguide laser, the gain region is in the active layer beneath the ridge, therefore, **a** in Fig.1.3 is the most favoured mode (TE_{00}) in this structure; with high enough gain, TE_{10} mode (**b**) is also a possible laser mode, but **c** or **d** certainly will not be the laser mode due to poor mode overlap with the gain region. During modelling, no TM mode is found to be supported by this structure. Therefore QT703R is a design in favour of only TE modes.

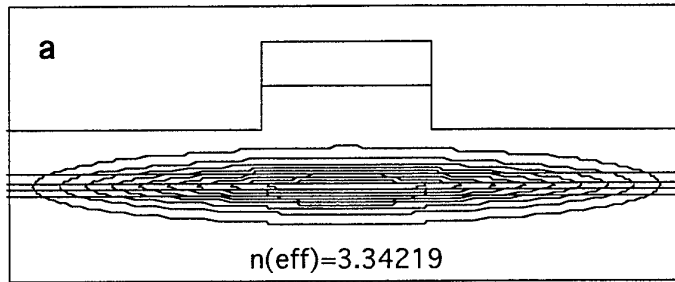
If the rib height is reduced to $1\text{ }\mu\text{m}$, from the results in Fig.1.4, quite different mode behaviours resulted: the structure still supports the TE_{00} mode, but predictably, a higher gain (or higher threshold current) is needed in order to compensate for the lower mode confinement factor. No other mode will be a laser mode in this structure due to the very low confinement factors of other guided modes.

If the rib width is reduced to $3\text{ }\mu\text{m}$, Fig.1.5 is obtained as the modelling results. Under this structure, again TE_{00} is the only laser mode supported, but with a further increase in threshold current. No other laser mode is possible due to the poor mode overlap with the gain region.

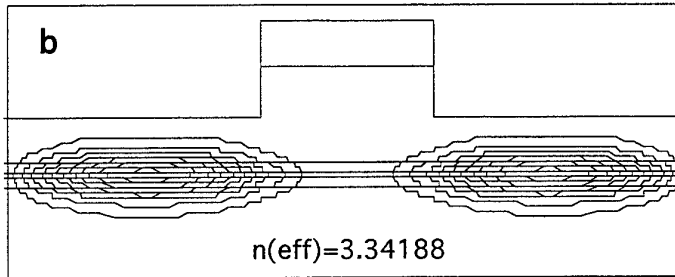
With very high rib designs as shown in Fig.1.6 where $w=5\text{ }\mu\text{m}$ and $t=1.5\text{ }\mu\text{m}$, the situation is quite different. Both TE and TM modes can lase, as well as the higher order modes. All modes in Fig.1.6 are likely to be laser modes, with the favourite order $TE_{00} > TE_{10} > TM_{00} > TE_{20}$. Under certain pumping condition, all these modes may appear in the far field pattern of the laser. We did observe such a multi-moded laser where due to the unsuccessful metal lift-off, the ridge width is slightly larger than designed, and due to non-uniform over etching, the ridge height is also larger.

From the modelling above, it is clear that with the same ridge width, larger rib height, or deeper trench etch tends to give better confinement to the guiding mode. Therefore, a lower threshold current should be expected. At the same time, it also provides better chance for higher order mode emission in a laser. When the etch depth reaches the core layer, multi-mode emission, including the TM mode is very likely to happen for a $5\text{ }\mu\text{m}$ ridge width laser. On the other hand, for a given rib height but different rib widths (Fig.1.4 and Fig.1.5), smaller rib width gives a worse mode confinement factor, but better lowest order mode performance. When $w=3\text{ }\mu\text{m}$ and $t=1.5\text{ }\mu\text{m}$, as shown in Fig.1.5 (c), only the TE_{00} mode is found to be a possible laser mode. Extensive modelling suggests that choosing the ridge width to be $3\sim 5\text{ }\mu\text{m}$ and the

$w=5, t=1 \mu\text{m}$; TE₀₀; 10% contour step



$w=5, t=1 \mu\text{m}$; TE₁₀; 10% contour step



$w=5, t=1 \mu\text{m}$; TE₂₀; 10% contour step

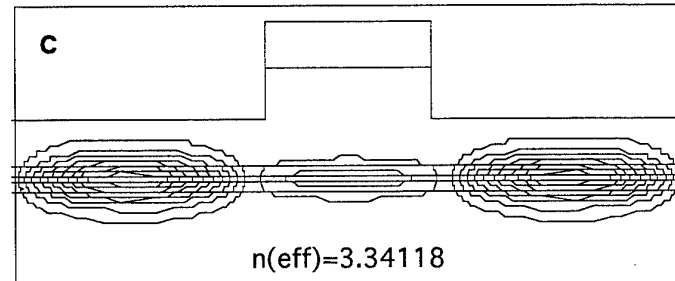
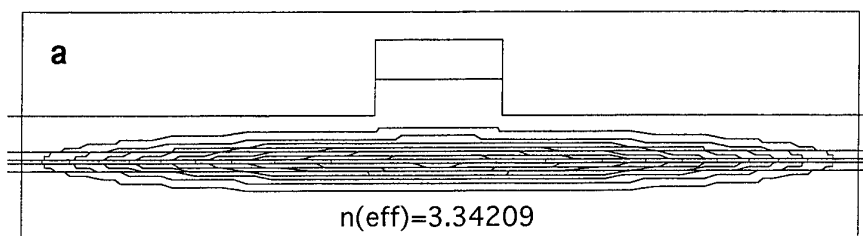
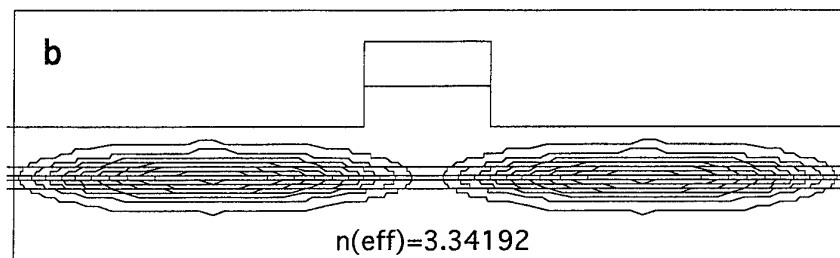


Fig.1.4. Field modelling results for QT703R with $w=5\mu\text{m}$, $t=1 \mu\text{m}$.

$w=3$, $t=1\text{ }\mu\text{m}$; TE₀₀; 10% contour step



$w=3$, $t=1\text{ }\mu\text{m}$; TE₁₀; 10% contour step



$w=3$, $t=1.5\text{ }\mu\text{m}$; TE₀₀; 10% contour step

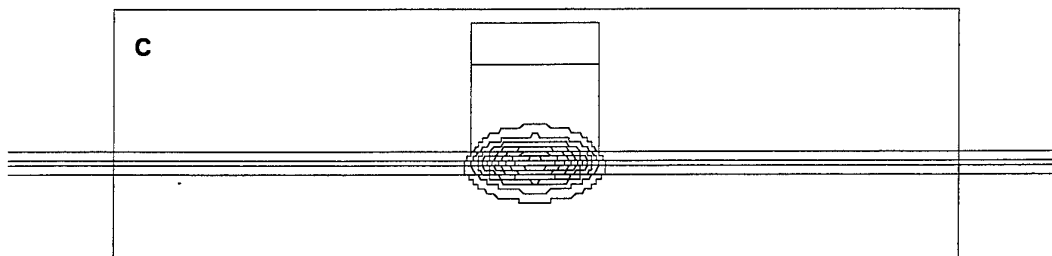


Fig.1.5. Field modelling results for QT703R with $w=3\text{ }\mu\text{m}$, $t=1$ and $1.5\text{ }\mu\text{m}$.

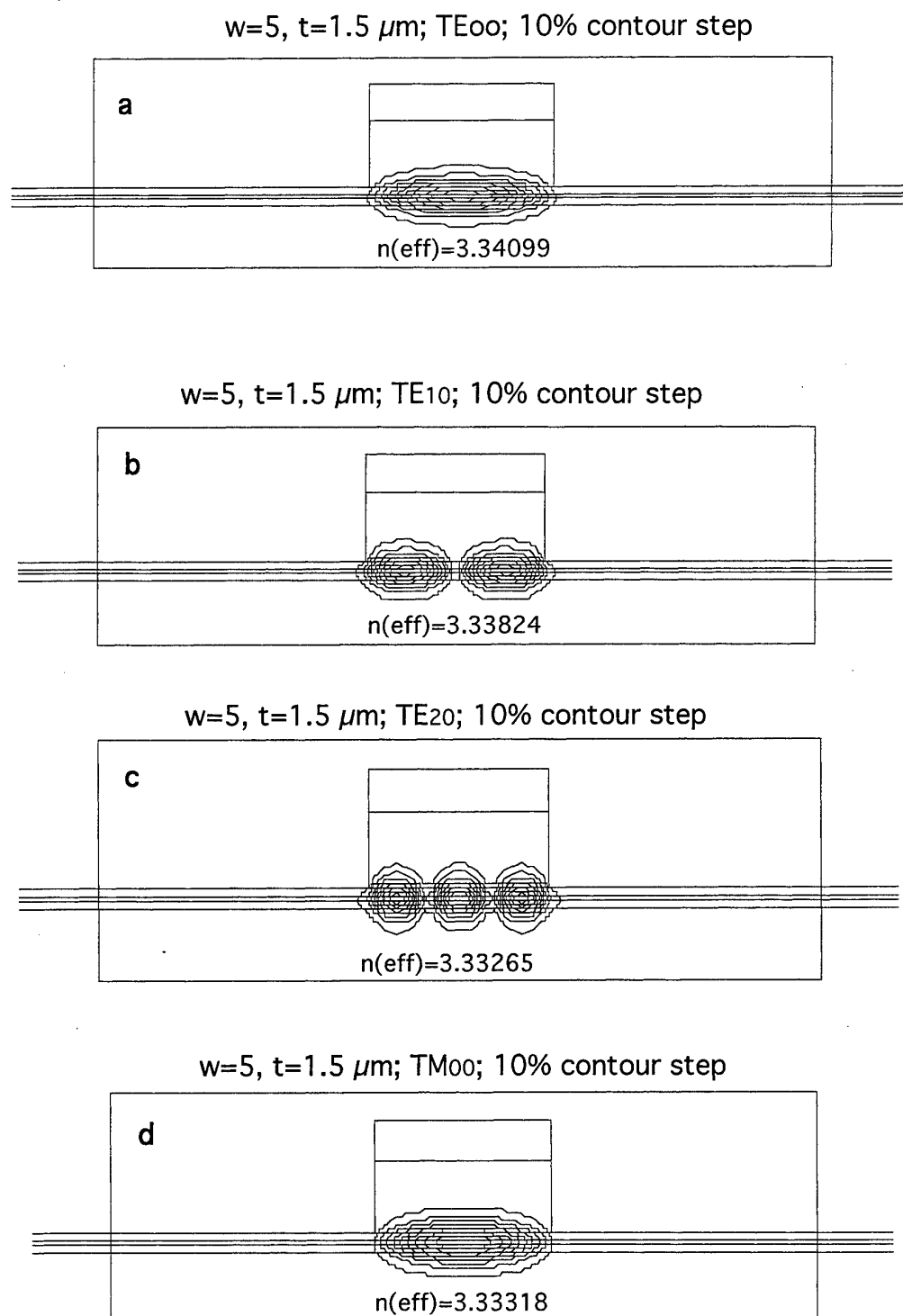


Fig.1.6. Field modelling results for QT703R with $w=5 \mu\text{m}$, $t=1.5 \mu\text{m}$.

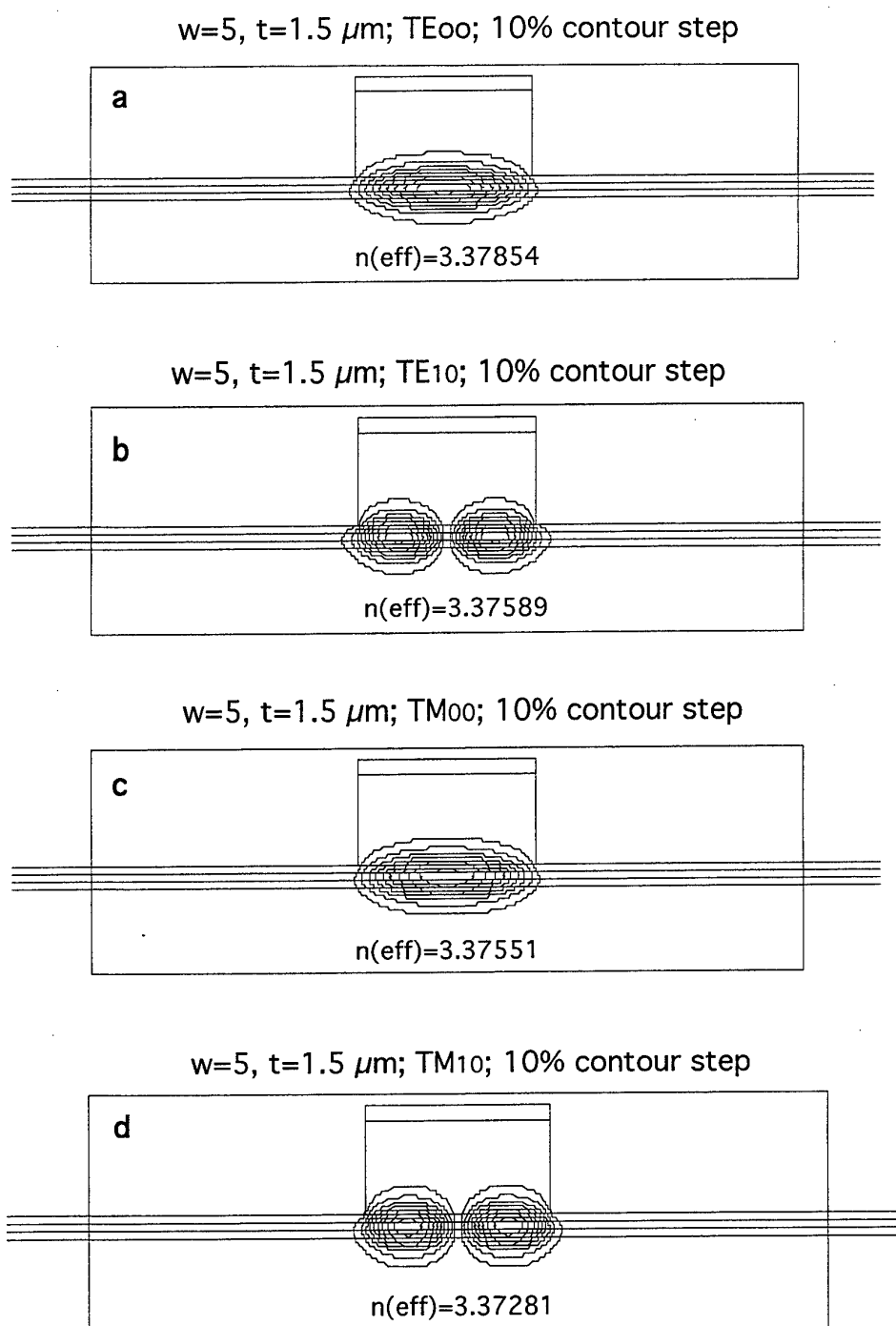


Fig.1.7. Field modelling results for QT787 with $w=5 \mu\text{m}$, $t=1.5 \mu\text{m}$.
In addition, TE₂₀ mode is supported by this guide.

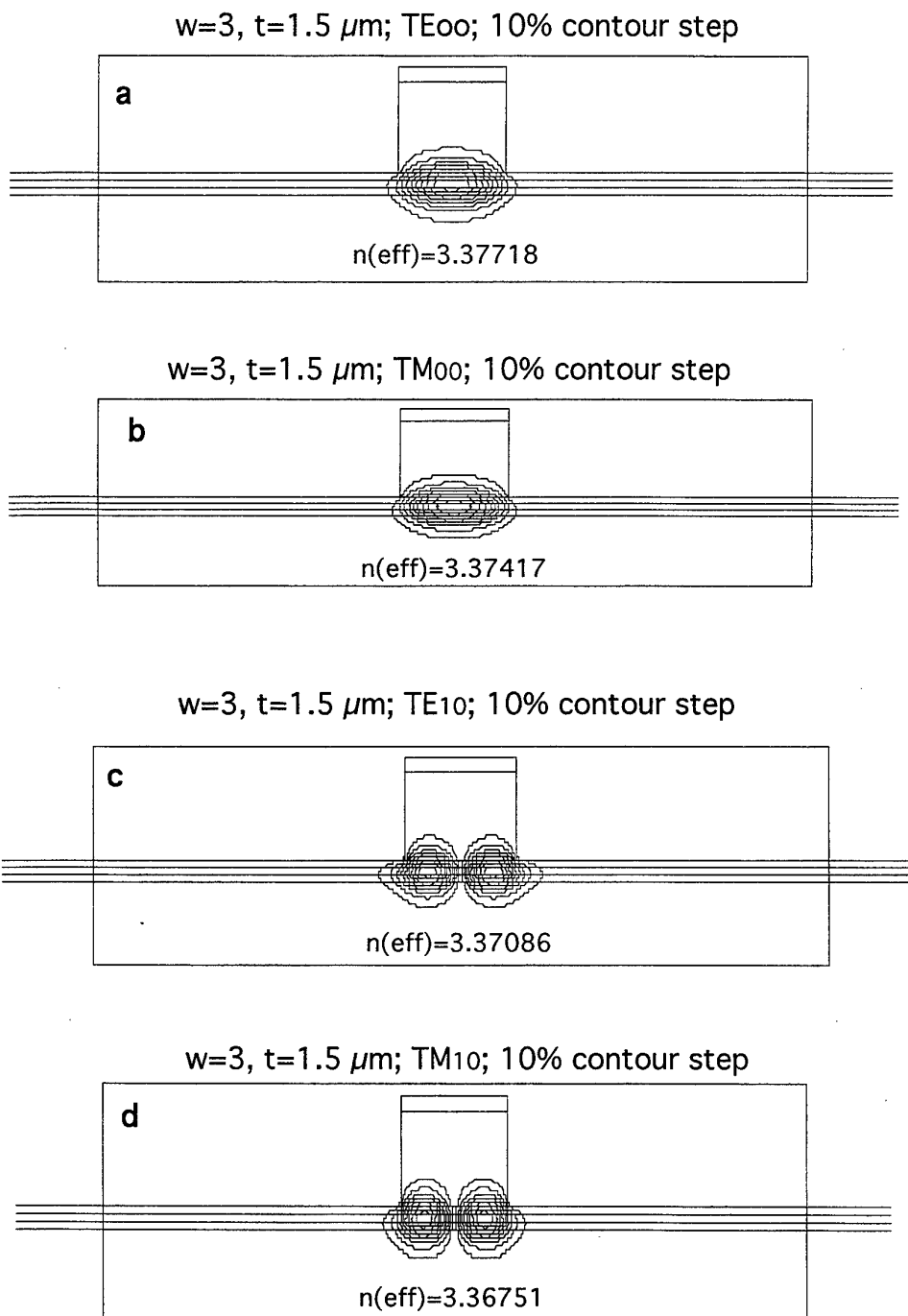


Fig.1.8. Field modelling results for QT787 with $w=3 \mu\text{m}$, $t=1.5 \mu\text{m}$.

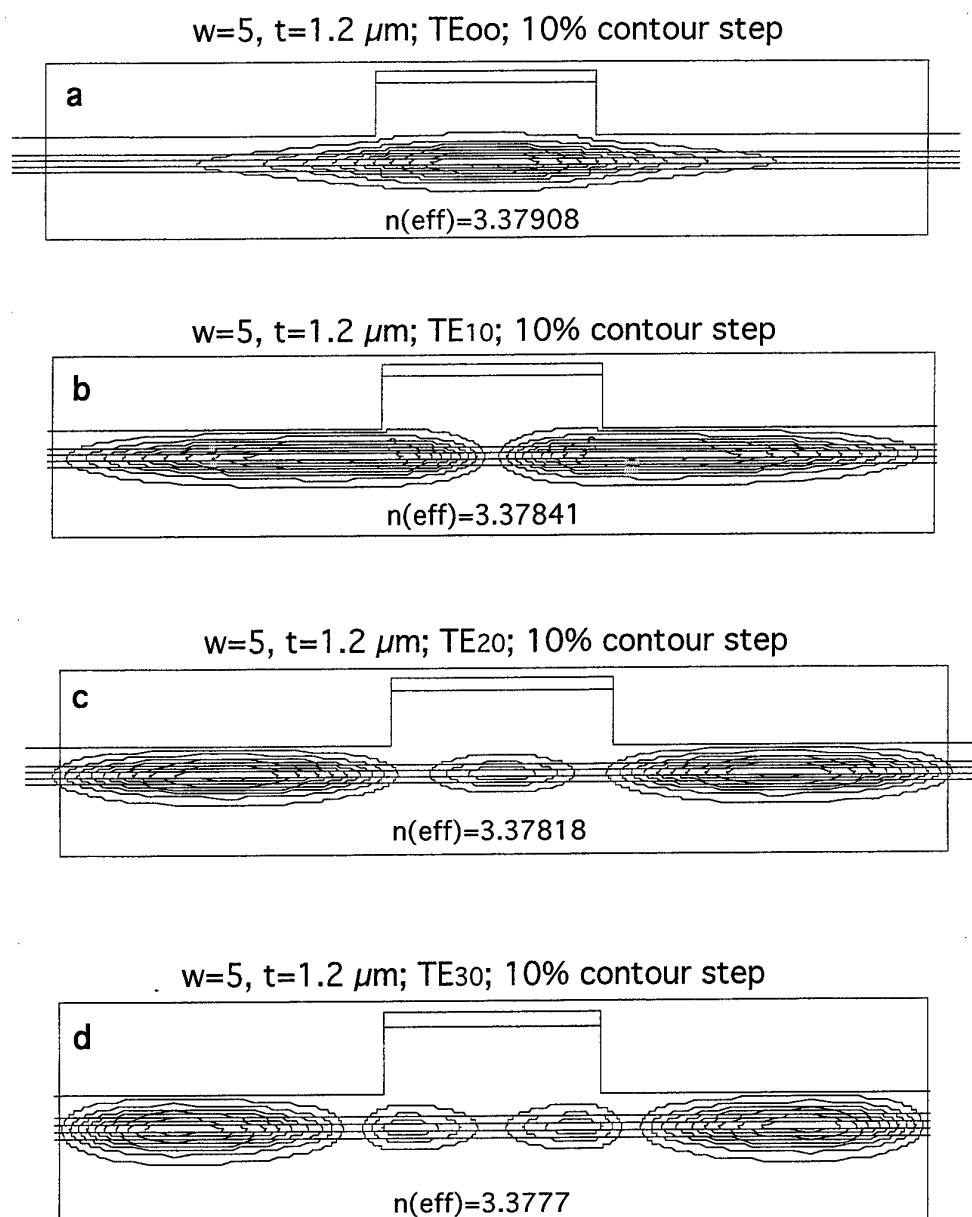


Fig.1.9. Field modelling results for QT787 with $w=5$ μm , $t=1.2$ μm . Laser will support only TE₀₀ mode, other modes are very unlikely to be supported in the laser cavity.

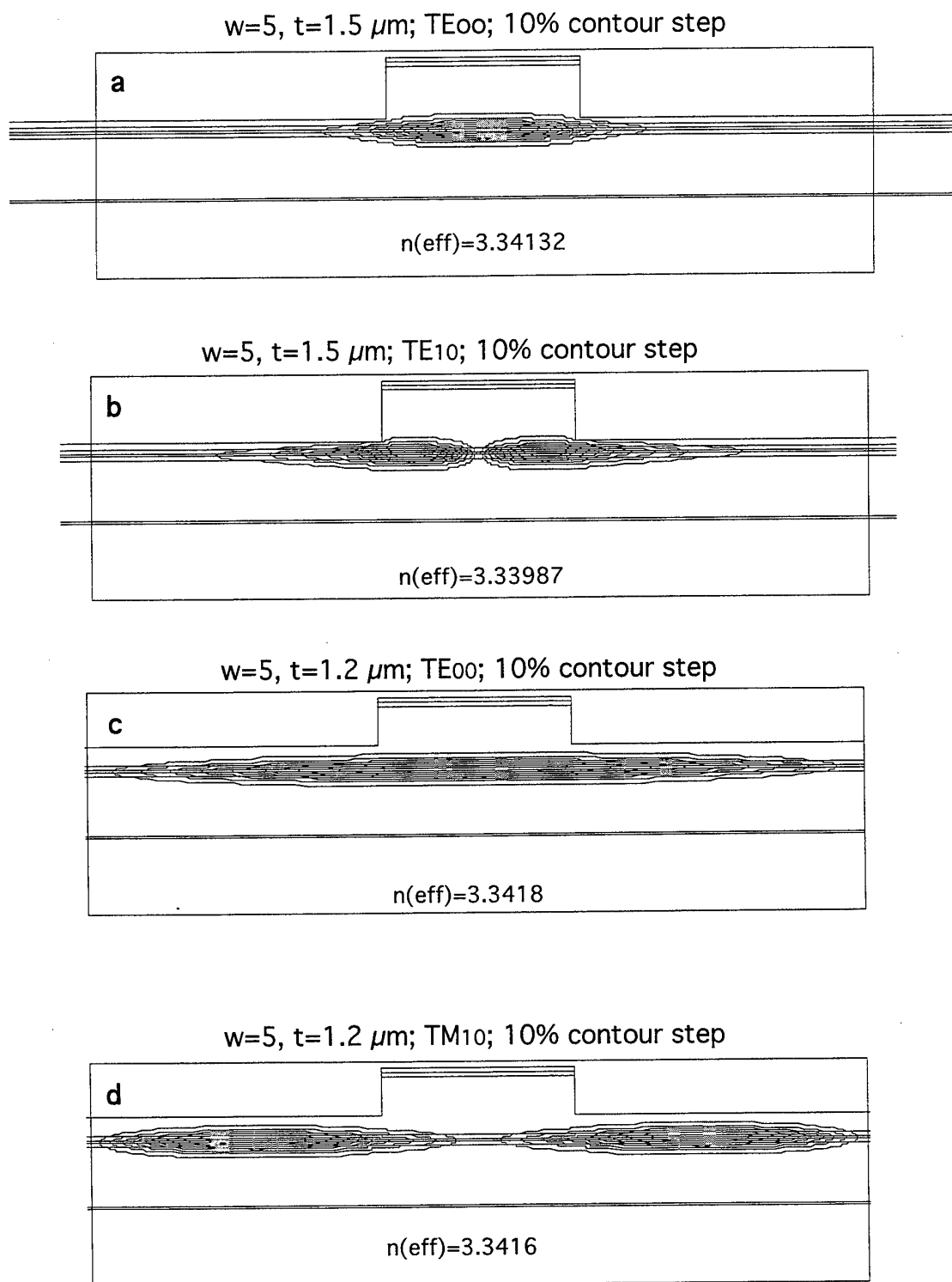


Fig.1.10. Field modelling results for QT862 with $w=5$ μm , $t=1.5$ and 1.2 μm . Only TE₀₀ mode is going to be a laser mode except that when $t=1.5$ μm , TE₁₀ is also a possible one.

ridge height to have its trench bottom $0.2\sim0.4\ \mu\text{m}$ above the waveguide core layer is the proper design for single mode operation.

Fig.1.7 to Fig.1.9 gives the modelling results for QT787. Comparing to QT703R, although the MQW active layer and the total thickness are of similar, the core thickness and the refractive index steps between the MQW region and the core layer, and between the core layer and the cladding layer, is quite different. QT787 has thicker core and smaller refractive index steps. The modelling predicts significant effects on laser performance. From Fig.1.7 and Fig.1.8, for a deep etched ridge, the laser will be a multi-moded, supporting TE_{00} , TM_{00} , TE_{10} , TM_{10} , and even TE_{20} as the laser emission mode, even if the ridge width is reduced to $3\ \mu\text{m}$. That means, thicker guiding core and smaller refractive steps tend to favor multi-mode emission. A proper etched ridge, as shown Fig.1.9, can still produce emission in a single TE_{00} mode.

Fig.1.10 is the modelling results for QT862. For a deep etch, similar results to QT703R (Fig.1.3) are found, except TE_{00} , TE_{10} is also a possible laser mode, but with smaller mode confinement factor due to a smaller core thickness. Lasing in TM or other higher order modes is found not to be possible.

QT863 has also been modelled. As with QT862, no TM modes are found supported by the structure. For $w=5\ \mu\text{m}$ and $t=1.6\ \mu\text{m}$, the TE_{10} mode is supported. It is clear that a deep etch to form the ridge should always be avoided.

Our modelling using FWave has been compared to the modelling carried out by Dr. Rachel Geatches and Dr. Susan Burke in University Wales College of Cardiff, based on the spectral index method^{13,14}, for the same ridge waveguide structure. The results are completely the same, proving that our modelling is credible. Based on our modelling, great care must be taken for ridge width and trench depth control during device processing.

1.2. The calculation of optical confinement factor

Optical confinement factor is defined as the fraction the optical energy guided in a guiding structure comparing to the total optical energy. The factor is important in the sense that any change in the waveguide can only have an effect on the whole optical field proportional to the energy retained in the waveguide.

To deduce an expression for optical confinement factor, let us start from a simple symmetric three layer slab waveguide shown schematically in Fig.1.11. The core or active layer of thickness d is surrounded on both side by cladding layers. If the cladding layers are sufficiently thick such that the optical field is largely confined within the three layers, for an actual structure, the remaining other layers can be ignored.

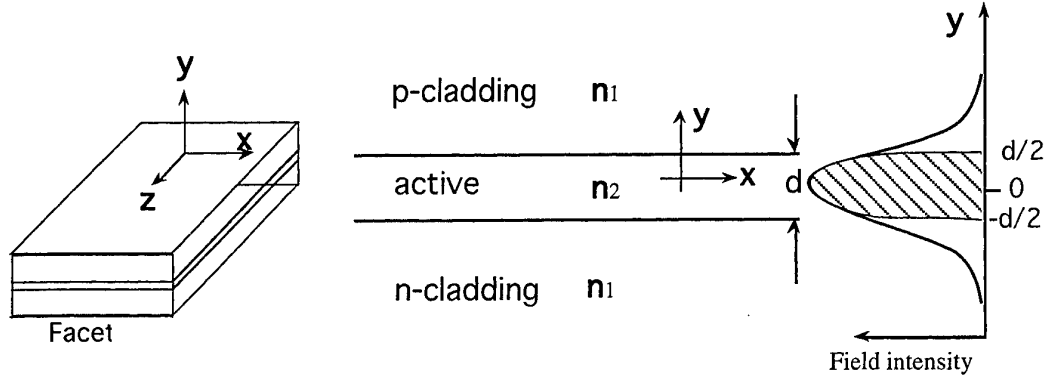


Fig.1.11 Three-layer slab waveguide model of a laser with refractive indices $n_2 > n_1$. The hatched region in the field distribution intensity represents the fraction of the mode within the active region.

The slab waveguide problem has been studied extensively¹⁵. It is found that this waveguide supports two sets of modes, the TE and the TM modes which are distinguished on the basis of their polarisation. For TE modes the electric field \mathbf{E} is polarised in the heterojunction plane along the x axis. For TM modes, it is the magnetic field \mathbf{H} polarised along x axis. Since the mode confinement in the y direction of a semiconductor laser is mainly due to the refractive index step at the heterostructure interface, the gain or loss can be treated as a small perturbation to the eigenvalue problem, hence, the dielectric constant $\epsilon(x, y)$ of (1.20) can be written in the form

$$\epsilon(x, y) = n_b^2 + \Delta\epsilon(x, y) \quad (1.29)$$

where n_b is the background (real) refractive index, constant for each layer. The small perturbation $|\Delta\epsilon| \ll n_b^2$ includes the loss and the contribution of external pumping.

By using first order perturbation theory,¹⁶ the eigenvalue given by n_{eff} becomes

$$n_{\text{eff}}(x) = n_e(x) + \Delta n_e(x) \quad (1.30)$$

where $n_e(x)$ is obtained by solving the unperturbed eigenvalue equation

$$\frac{d^2\phi}{dy^2} + \kappa_0^2 [n_b^2(y) - n_e^2(x)]\phi = 0 \quad (1.31)$$

and the perturbation Δn_e is obtained using

$$2n_e \Delta n_e(x) = \frac{\int_{-\infty}^{\infty} \Delta \epsilon(x,y) \phi^2(y;x) dy}{\int_{-\infty}^{\infty} \phi^2(y;x) dy} \quad (1.32)$$

Since $\Delta \epsilon(x,y)$ is constant within each layer, (1.32) can be simplified to be

$$\Delta n_e(x) = \frac{1}{2n_e} \sum_j \Gamma_j(x) \Delta \epsilon_j(x) \quad (1.33)$$

where the sum is over the number of layers, $\Delta \epsilon_j$ is the dielectric perturbation of j th layer, and

$$\Gamma_j(x) = \frac{\int_{-\infty}^{\infty} \phi^2(y;x) dy}{\int_{-\infty}^{\infty} \phi^2(y;x) dy} \quad (1.34)$$

is the fraction of the mode energy contained in the j th layer, and is referred to as the confinement factor if the layer is the active layer. If the active layer is not laterally uniform in thickness, both Γ_j and the effective index n_e vary with x . The average confinement factor for this case is

$$\Gamma = \frac{\int_{active} \Gamma_{active}(x) dx}{\int_{active} dx} \quad (1.35)$$

For a simple three-layer slab laser as shown in Fig.1.11, the unperturbed field is uniform along x axis, therefore

$$\Gamma = \frac{\int_{-d/2}^{d/2} \phi^2(y) dy}{\int_{-\infty}^{\infty} \phi^2(y) dy} \quad (1.36)$$

where $\phi(y)$ is the solutions of (1.31). If the even and odd solutions of (1.31) can be treated separately,¹⁷ the mode analysis is simplified considerably. For the even TE modes, a general solution of (1.31) is of the form

$$\phi(y) = \begin{cases} A_e \cos(\kappa y) & \text{for } |y| \leq d/2 \\ B_e \exp[-\gamma(|y| - d/2)] & \text{for } |y| \geq d/2 \end{cases} \quad (1.37)$$

where

$$\kappa = \kappa_0 (n_2^2 - n_e^2)^{1/2} \quad (1.38)$$

$$\gamma = \kappa_0 (n_e^2 - n_1^2)^{1/2} \quad (1.39)$$

are both real. n_2 and n_1 are the material refractive indices for the active and cladding layers, respectively, with $n_2 > n_1$. The continuity of ϕ and $d\phi/dy$ at $|y|=d/2$ requires that

$$B_e = A_e \cos(\kappa d/2) \quad (1.40)$$

$$\gamma B_e = \kappa A_e \sin(\kappa d/2) \quad (1.41)$$

which result the eigenvalue equation

$$\gamma = \kappa \tan(\kappa d/2) \quad (1.42)$$

whose solution yield the effective mode index n_e . In general, multiple solutions are obtained corresponding to different even TE modes.

Similarly, for the odd TE modes, a general solution and the eigenvalue equation is obtained as

$$\phi(y) = \begin{cases} A_e \sin(\kappa y) & \text{for } |y| \leq d/2 \\ B_e \exp[-\gamma(|y| - d/2)] & \text{for } |y| \geq d/2 \end{cases} \quad (1.43)$$

$$\gamma = -\kappa \cot(kd/2) \quad (1.44)$$

The solutions of (1.44) yield the effective mode index n_e for odd TE modes. For all guided modes, the relation of $n_2 > n_e > n_1$ is always satisfied. From (1.38) and (1.39),

$$\kappa^2 + \gamma^2 = \kappa_0^2 (n_2^2 - n_1^2) \quad (1.45)$$

which describes a circle in the κ - γ plane. Together with (1.42) or (1.44), a series κ_m γ_m for the m th order TE mode is obtained. That multiple solutions occur is due to the periodic nature of trigonometric functions. The allowed waveguide mode can be determined by noting that if $\gamma \leq 0$, field distribution ϕ in (1.37) and (1.44) grows exponentially, and therefore is not a possible mode. Only the solution with $\gamma \geq 0$ represents a possible mode.

By using (1.37) and carrying out the integration of (1.36), the confinement factor for the m th TE even mode is

$$\Gamma_m = \frac{1 + 2\gamma_m d/D^2}{1 + 2/\gamma_m d} \quad (1.46)$$

$$\text{and } D^2 = \kappa_0^2 d^2 (n_2^2 - n_1^2) \quad (1.47)$$

is the normalised waveguide thickness.

For a semiconductor laser, it is always desirable to make it works with only the fundamental TE mode, that is the lowest even TE mode. For this fundamental TE mode, (1.46) can be further simplified to

$$\Gamma_0 \cong \frac{D^2}{2 + D^2} \quad (1.48)$$

which is so simple that for a certain three-layer slab structure, its fundamental TE mode confinement factor is readily calculable.

For normal MQW heterostructure lasers as modelled in the last section, the active layer is the MQW region, but the guiding layer including upper and lower core layers,

as shown in Fig.1.12. As far as the confinement factor concerned, to a good

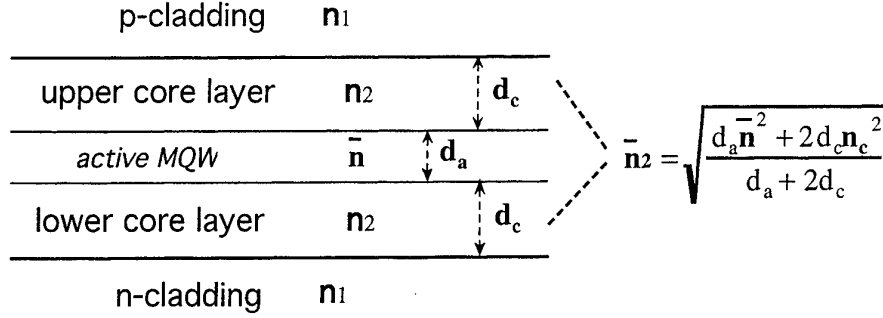


Fig.1.12 General MQW separate confinement heterostructure (SCH) laser with five-layer structure can be treated as three-layer slab structure with a weighted average index instead of \bar{n}_2 .

approximation, this structure can be treated as an equivalent three-layer slab structure: the core region comprising the MQW layer and the upper and lower core layers with an equivalent refractive index taken from the three core layers weighted average. Based on this approximation, the field distribution for TE even mode is regarded as a single cosine function over the whole guiding region including MQW region, but as a decaying exponential function outside the core, as expressed in (1.37). The confinement factor of the MQW active region is

$$\Gamma_{MQW} = \frac{\int_{-d_a/2}^{d_a/2} \phi^2 dy}{\int_{-\infty}^{\infty} \phi^2 dy} \quad (1.49)$$

where d_a is the thickness of MQW region. (1.49) can be further deduced into

$$\Gamma_{MQW} = \frac{\int_{-d/2}^{d/2} \phi^2 dy \times \frac{\int_{-d_a/2}^{d_a/2} \phi^2 dy}{\int_{-d/2}^{d/2} \phi^2 dy}}{\int_{-\infty}^{\infty} \phi^2 dy} = \Gamma_0 \times \frac{\int_{-d_a/2}^{d_a/2} \phi^2 dy}{\int_{-d/2}^{d/2} \phi^2 dy} = \Gamma_0 \times \Gamma_a \quad (1.50)$$

where

$$\Gamma_0 = \frac{\int_{-d/2}^{d/2} \phi^2 dy}{\int_{-\infty}^{\infty} \phi^2 dy} \quad (1.51)$$

is the confinement factor of the whole waveguide, $d=d_a+2d_c$ is the thickness of the guide as shown in Fig.1.12, and

$$\Gamma_a = \frac{\int_{-d_a/2}^{d_a/2} \phi^2 dy}{\int_{-d/2}^{d/2} \phi^2 dy} \quad (1.52)$$

is the fraction that energy confined in MQW region comparing to the whole waveguide. By using (1.37) to (1.47), it is not difficult to evaluate (1.50). Under this

situation, the index of the whole waveguide should be substituted by the weighted average value in this region

$$\bar{n}_2 = \sqrt{\frac{d_a \bar{n}^2 + 2d_c n_2^2}{d_a + 2d_c}} \quad (1.53)$$

$$\text{and} \quad D^2 = \kappa_0^2 d^2 (\bar{n}_2^2 - n_1^2) \quad (1.54)$$

where \bar{n} is the weighted average index of MQW region obtained by (1.28), n_2 is the index of upper and lower core layers, and \bar{n}_2 the weighted average index of guiding layer. Finishing the integration in (1.53) by using (1.37), we have for TE even modes

$$\Gamma_a = \frac{\sin(\kappa d_a) + \kappa d_a}{\sin(\kappa d) + \kappa d} \quad (1.55)$$

and

$$\Gamma_{MQW} = \frac{1 + 2\gamma d / D^2}{1 + 2 / \gamma d} \cdot \frac{\sin(\kappa d_a) + \kappa d_a}{\sin(\kappa d) + \kappa d} \quad (1.56)$$

By using (1.42), (1.45) and (1.54), γ and κ are obtained numerically for each order of TE even mode, therefore Γ_{MQW} can be obtained explicitly. Only the solutions with γ real and > 0 are meaningful, therefore κ should be in the range $-D/d < \kappa < D/d$.

The fundamental TE-even mode and its confinement factor of the MQW active layer for the structure in Fig.1.2 have been calculated according to the theory stated above. Fig.1.13 is the results for QT703R and QT787, and Fig.1.14 is that for QT862 and QT863. All calculation is for a wavelength of 850 nm.

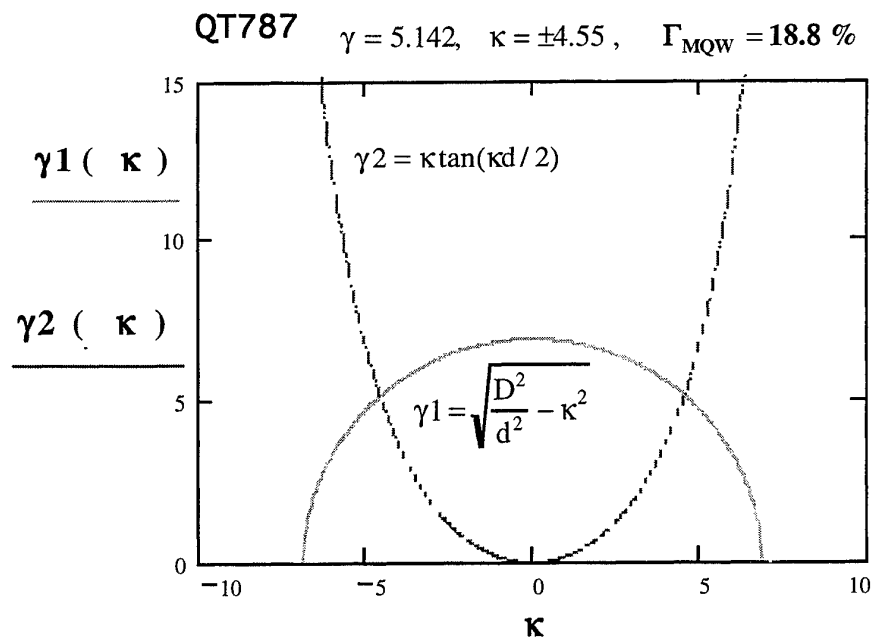
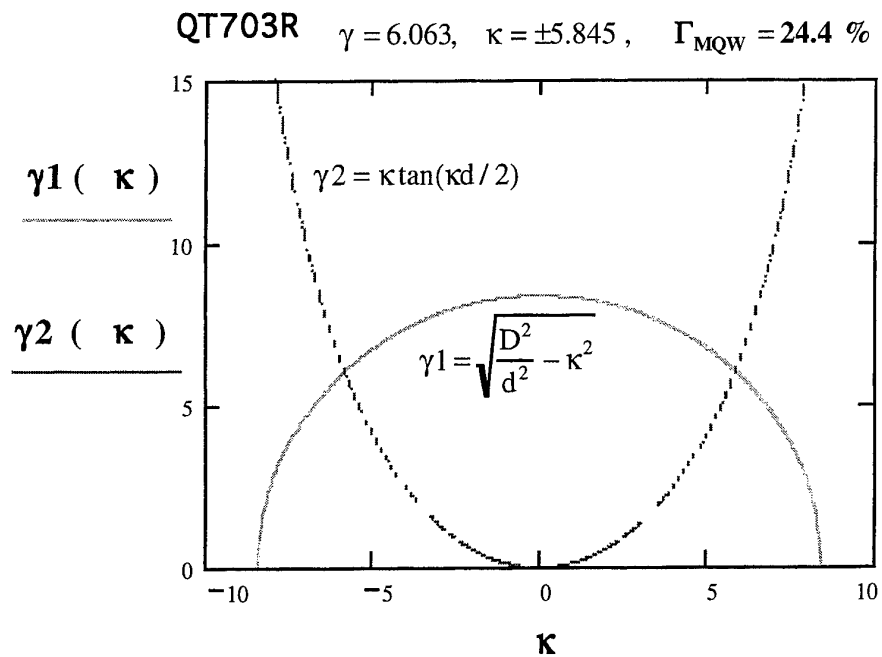


Fig.1.13 TE-even mode and MQW active layer confinement factor calculated for QT703R and QT787.

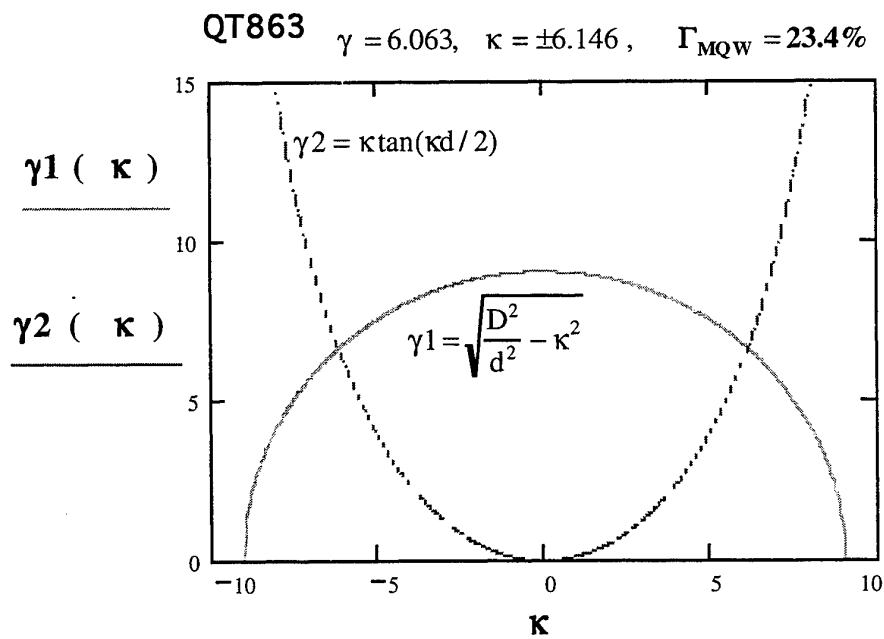
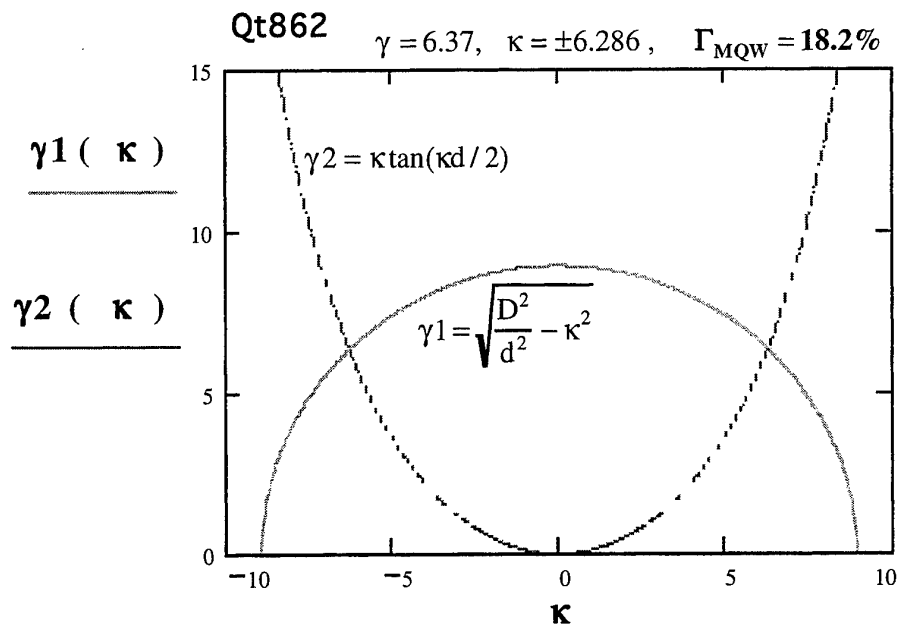


Fig.1.14 TE-even mode and MQW active layer confinement factor calculated for QT862 and QT863.

1.3. The calculation of absorption spectrum and refractive index from experimental transmission spectra

The simple method of determining absorption spectra involves the measurement of transmission, which is the ratio of transmitted intensity to input intensity

$$T = T_0 \exp(-\alpha d) \quad (1.57)$$

where α is the absorption coefficient, d the thickness of absorber and T_0 the ideal transmission when the reflected energy is subtracted from the total input energy (normalised to unity). With GaAs MQW structures, there are two obstacles to the accurate measurement of absorption. Firstly, the GaAs substrate is absorptive at the edge of exciton peak of the MQW, so the substrate must be completely removed from the optical path. Fortunately, for GaAs material system, highly selective etches, both dry and wet^{18,19} are readily available which remove GaAs in preference of to AlGaAs. However, after GaAs substrate is removed, the remaining p-i-n MQW structure is only 2~3 μm in thickness with very smooth parallel front and rear surface. Both surface have roughly 30% reflectivity, form a Fabry-Perot cavity and cause strong interference to the measured transmission spectrum, as shown in Fig.1.15. This is the second obstacle to obtain a true absorption spectrum.

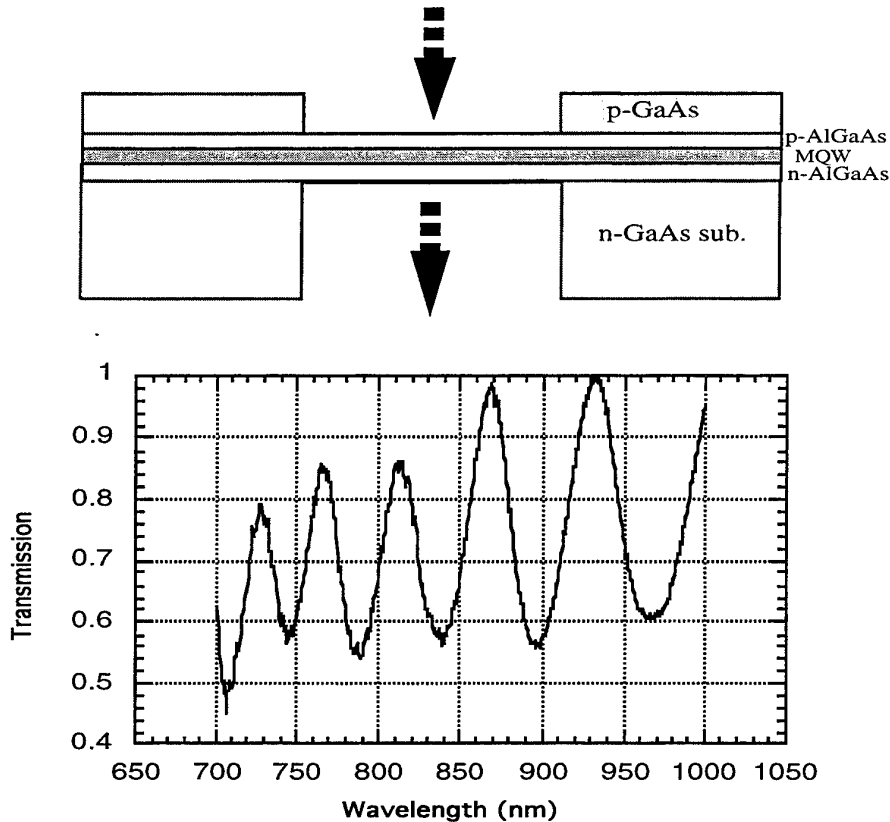


Fig.1.15 A typical measured transmission spectrum in the presence of F-P cavity effect.

Even after depositing an anti-reflection coating on front and rear surfaces, the residual reflection is still strong enough to cause F-P interference in the transmission spectrum, making it still difficult to work out the true absorption. Therefore, we have to consider the situation when both the absorption and the FP interference effects are present and we wish to calculate α from the transmission spectrum. For an absorber cavity in the air, the governing equation for intensity transmission is not difficult to work out:

$$T = \frac{T_0^2 e^{-\alpha d}}{1 + R^2 e^{-2\alpha d} - 2R \cdot e^{-\alpha d} \cdot \cos(2\delta)} \quad (1.58)$$

where R is the reflectivity of front or rear surface (regarded as equal), d is the thickness of absorptive layer in the medium, and $\delta = 2\pi n_{qw} L / \lambda$ is the phase shift for passage through the medium with refractive index n_{qw} and total thickness L . (1.58) can be further simplified as

$$T = \frac{T_0^2 e^{-\alpha d}}{(1 - R e^{-\alpha d})^2 + 4R \cdot e^{-\alpha d} \cdot \sin^2 \delta} \quad (1.59)$$

Obviously, the phase shifting introduces the periodic variation in the spectrum. The maximum or minimum happens when

$$\delta = m\pi, \quad T_{\max} = \frac{T_0^2 e^{-\alpha d}}{(1 - R \cdot e^{-\alpha d})^2} \quad (1.60)$$

and

$$\delta = \frac{(2m+1)\pi}{2}, \quad T_{\min} = \frac{T_0^2 e^{-\alpha d}}{(1 + R \cdot e^{-\alpha d})^2} \quad (1.61)$$

where m is an integer. Divided (1.60) by (1.61), we have

$$\frac{T_{\max}}{T_{\min}} = \frac{(1 + R \cdot e^{-\alpha d})^2}{(1 - R \cdot e^{-\alpha d})^2} \quad (1.62)$$

in the wavelength far beyond 870nm, the absorption coefficient is zero, therefore

$$\frac{T_{\max}}{T_{\min}} = \frac{(1 + R)^2}{(1 - R)^2} \Big|_{\lambda > 870nm} \quad (1.63)$$

From (1.63), we can work out the reflectivity R . By using Fig.1.15, we obtain $R=12.5\% \sim 14\%$ in wavelengths beyond 870 nm, which is also a slow by varying parameter versus wavelength. From (1.60), it is also realised that if there is no absorption, $T_{\max}=1$, because $1-R=T_0$. We can therefore scale the whole spectrum to its absolute T_{\max} transmission value, as we already did in Fig.1.15. For the example above, we also have $T_0=86\% \sim 87.5\%$.

The last step is to work out the δ from measured transmission spectrum. We know the phase at maximum and minimum, we can deduce the phase between them by mathematical interpolation method. From Fig.1.15, we have the phase spectrum shown in Fig.1.16. We can then have the phase data corresponding to

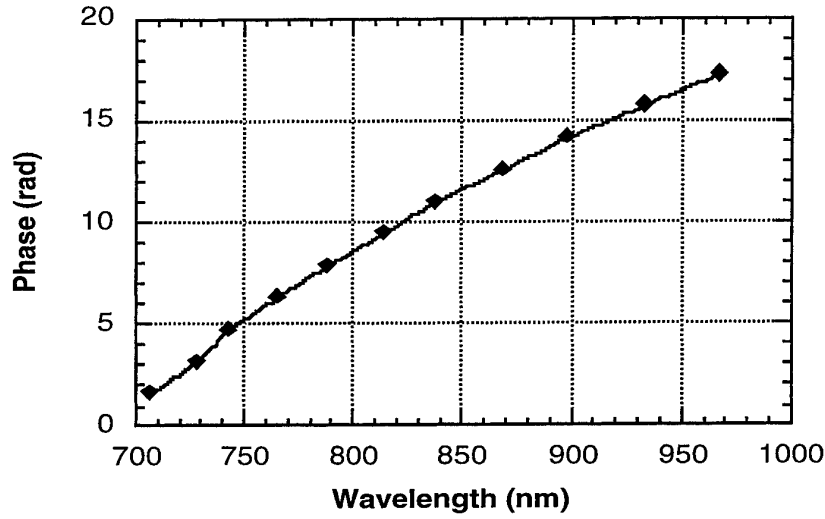


Fig.1.16 Phase data and the interpolation (solid line) result for the curve in Fig.1.15.

each wavelength, and finally, calculate the absorption spectrum by equation (1.59). Fig.1.17 is the result of absorption spectra calculated from measured transmission spectra for sample QT703R under different reverse biases.

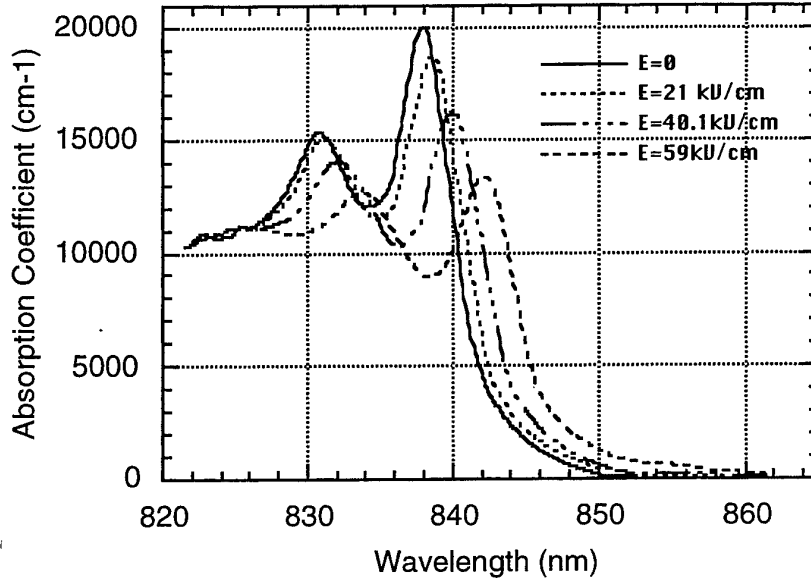


Fig.1.17 Absorption spectra calculated from transmission measurements for sample QT703R. Different field strength were applied to the sample (zero field corresponding to a positive bias).

It is now straight forward to calculate absorption change and at last, the refractive index change under different field by using the Kramers-Kronig relation

$$\Delta n(\lambda, E) = \frac{\lambda^2}{2\pi^2} P \int_0^\infty \frac{\Delta \alpha(\lambda', E) d\lambda'}{\lambda'^2 - \lambda^2} \quad (1.64)$$

where P is the Cauchy principal value of the integral. From Fig.1.18, the absorption change spectra, it is noticed that changes in the wavelength range far from the exciton peak (838nm) both tend to zero, therefore, their contribution to the integral is negligible. It is convenient to obtain index change from Fig.1.18 by numerical integration techniques. The result is shown in Fig.1.19.

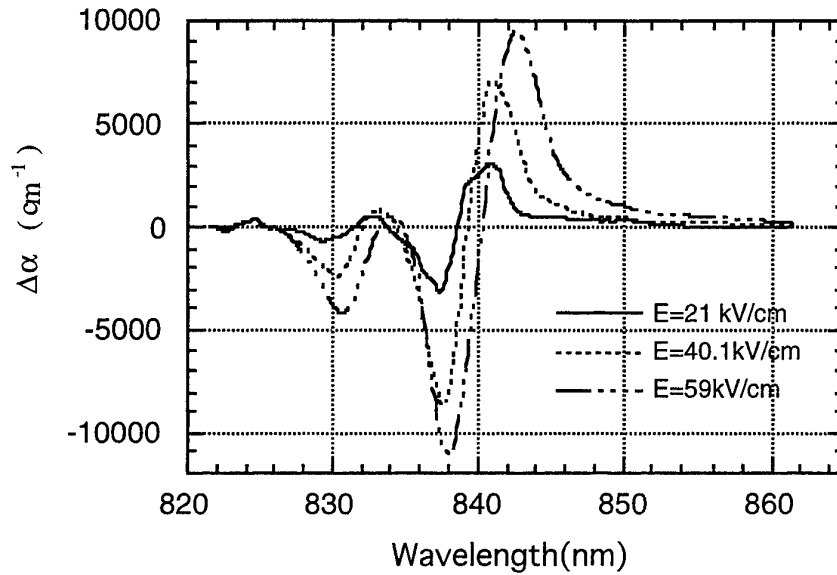


Fig.1.18 Absorption change spectra calculated from transmission measurements for sample QT703R. Field strengths are relative to zero field (corresponding to a positive bias).

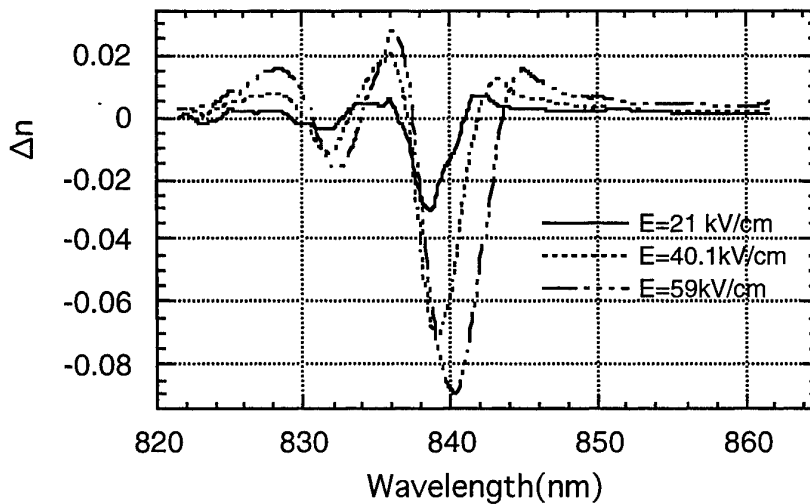


Fig.1.19 Refractive index change spectra calculated from transmission measurements for sample QT703R. Field strengths are relative to zero field (corresponding to a positive bias).

1.4. Calculations relating to tuning performance

As we discussed in the report of first year (Section 2.1.2), the refractive index change due to QCSE is very sensitive to the operating wavelength. As a tuning mechanism for use in an integrated tunable laser, some trade-off has to be made. Hence it is necessary to examine the tuning in more detail even though nominally it provides much larger refractive index changes compared to carrier induced effects. Fig.1.19 is the experimental refractive index change spectra under different electric field for the structure of QT703R. As can be seen, index change varies with wavelength violently, especially at wavelength centred about the exciton peak of the MQW structure. At those wavelengths, index changes even including opposite sign (from -2.5% to +0.5%), which means, no uniform tuning response is possibly achievable within these wavelengths, therefore, first of all tuning should not be performed across this wavelength range. Also the absorption and absorption change in this range are too high to have good power stability during tuning. Comparing with carrier induced effects, where the refractive index change variation with wavelength is quite smooth, this is the drawback of QCSE. The solution is to make the tuning work at the red side of MQW material absorption spectrum where the absorption is low and the refractive index change with field is positive and smaller (maximum about 0.5%). More importantly, both the absorption and the refractive index change with wavelength is quite smooth. This is exactly what is desired.

Fortunately, when the gain section is pumped towards its threshold condition, the high carrier density results in band gap reduction,²⁰ and the lasing wavelength is about 10nm longer than the exciton peak. This means that sharing a single cavity, the working wavelength in the tuning section locates at the red side of the exciton peak. Further lower and smoother absorption and refractive index change variations with wavelength are achievable by intentionally shifting the exciton peak of the tuning section toward the shorter wavelength side (blue shift), which can be done by the techniques of band gap tuning or band gap shifting.

Due to the large current density in the gain section, lateral carrier diffusion to the reverse biased tuning section because of the carrier density difference between the two sections may be an inevitable result. As ion implantation is adopted as the isolating method between the two sections, the implanted section will provide more than 1 M Ω resistance between them. The fact is that the high resistivity region is produced by the presence of large amount carrier trapping centre due to the lattice disordering (H^+ implanted) or impurity doping effect (deep energy level, O^+ implanted). The carrier trapping is so effective that the ion implanted isolation can

even be used to produce planar stripe lasers and other devices. This implies most laterally diffused carrier will be blocked by the ion implanted carrier trapping region. It is generally realised that as the carrier trap centre is normally a non-radiative recombination centre, one should avoid producing such a region within the active layer, otherwise the cavity loss will be extremely high and require much larger gain to compensate for it. Therefore, lateral carrier diffusion via the active layer is still inevitable even though the diffusion via the top contact and cladding layers is totally blocked. It is necessary to see how this diffusion will influence the pure QCSE tuning.

Illustrated in Fig 1.20, it is supposed that there is no carrier diffusion except in the active MQW layer which is treated as a whole. Let us calculate the carrier density presented in the tuning section due to this diffusion current I_2 .

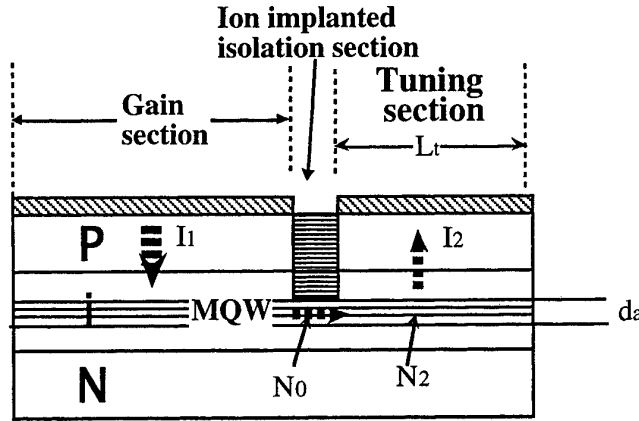


Fig. 1.20. 2-section laser with lateral carrier diffusion presented.

Suppose N_2 is the carrier density in the tuning section due to lateral diffusing, and N_0 is the carrier density just beneath ion implantation region due to lateral diffusion, then

$$I_2 = e \cdot N_2 \cdot v_2 \cdot A_2 = e \cdot N_0 \cdot v_0 \cdot A_0 \quad (1.65)$$

where e is electron charge, v is the diffusion (beneath implanted region) or drifting velocity of the carrier and A the cross sectional area perpendicular to the current direction. If the MQW thickness is d_a , ridge width is w and the tuning section length is L_t , then

$$A_2 = L_t \cdot w \quad (1.66)$$

$$A_0 = w \cdot d_a \quad (1.59)$$

and then

$$N_2 = \frac{I_2}{e \cdot v_2 \cdot A_2} = \frac{I_2}{e \cdot v_2 \cdot L_t \cdot w} \quad (1.68)$$

$$N_0 = \frac{I_2}{e \cdot v_0 \cdot A_0} = \frac{I_2}{e \cdot v_0 \cdot w \cdot d_a} \quad (1.69)$$

are the equations to estimate the carrier densities. As an example, if $I_2=0.1\text{mA}$, which is quite possible in an actual device, and we chose $v_0 \approx 10^7 \text{ cm/s}$, $v_2 \approx 2 \times 10^7 \text{ cm/s}$, $w=5 \mu\text{m}$, $L_t=300 \mu\text{m}$, $d_a=0.1 \mu\text{m}$, we have $N_2 \approx 2 \times 10^{12} \text{ cm}^{-3}$ and $N_0 \approx 1.3 \times 10^{16} \text{ cm}^{-3}$.

From the result above, it seems the diffused carrier density in the tuning cavity is too small to give important free carrier absorption in this section, but the carrier density in the bottle-neck region which is beneath the implanted region and within the cavity, could be very high and it is possible to have significant free carrier absorption. It is also noticeable that a small current variation could produce a large carrier density change within this area. Reducing the gap between the two section will decrease the loss, also properly controlled ion implantation into the active layer is a possible solution.

Another important factor that need to be considered is the photo-generated carrier effect on the tuning section: whether the photo-generated current is big enough to produce thermal effect in the tuning section, and whether the photo-generated carrier density high enough to cause large free carrier absorption loss. This consideration is important as the two sections share a single optical cavity and the optical field fills everywhere along the cavity. We can treat the tuning section as a laterally illuminated MWQ p-i-n photodetector in which its cut-off wavelength corresponds to GaAs cut-off wavelength $0.87\mu\text{m}$. As stated above, the actual lasing wavelength is about 10 nm longer than its exciton peak and therefore is quite near to the cut-off wavelength if the exciton peak is around 830-840 nm. Hence a low sensitivity at the lasing wavelength should be expected for this photodiode. The photo-generated current can be written as:

$$I_p = \Gamma_{\text{MQW}} \cdot P_o \cdot R_f \quad (1.70)$$

where Γ_{MQW} is the confinement factor of the MQW region, P_o is optical power inside the cavity (identical facets reflectivity is assumed) and R_f is the photodetector responsivity at the incident light wavelength. A numerical example is: $\Gamma_{\text{MQW}}=20\%$, $P_o=10\text{mW}$ (5mW/facet) and $R_f=0.1 \text{ mA/mW}$, $I_p=0.2 \text{ mA}$ is obtained, which is not big enough to produce thermal effect in the tuning section. By using (1.68) regarding $I_2=I_p$, $N_2 \approx 4 \times 10^{12} \text{ cm}^{-3}$, still too small to cause free carrier absorption loss. It is worthwhile to point out that, as $I_p \propto 1-e^{-\alpha d}$, and α increases with bias under the lasing wavelength due to the exciton peak shifts to red side with bias, R_f also increases with bias, resulting in a possible sharp increase in I_p . Once this happens, the thermal effect may be no longer negligible. To avoid this from happening, shifting the

working wavelength in the tuning section to a longer wavelength by blue shifting the exciton peak is a solution.

In order to achieve a large enough tuning range, a suitable tuning section length should be chosen. The phase shift in the tuning section can be written as

$$\Delta\Phi = \Gamma_{\text{MQW}} \cdot \Delta n \cdot L_t \cdot 2\pi/\lambda$$

where Γ_{MQW} is the confinement factor of the MQW structure, Δn is the refractive index change of the MQW, L_t is the length of the tuning section. For achieving a π phase shift, the tuning section length required is shown in Fig.1.21. The parameters adopted during calculation is as follows: $n=3.6$, $\lambda=0.85 \mu\text{m}$, $\Gamma_{\text{MQW}}=20\%$, $\Delta n/n=0.1\%\sim 0.5\%$ from Fig.1.19.

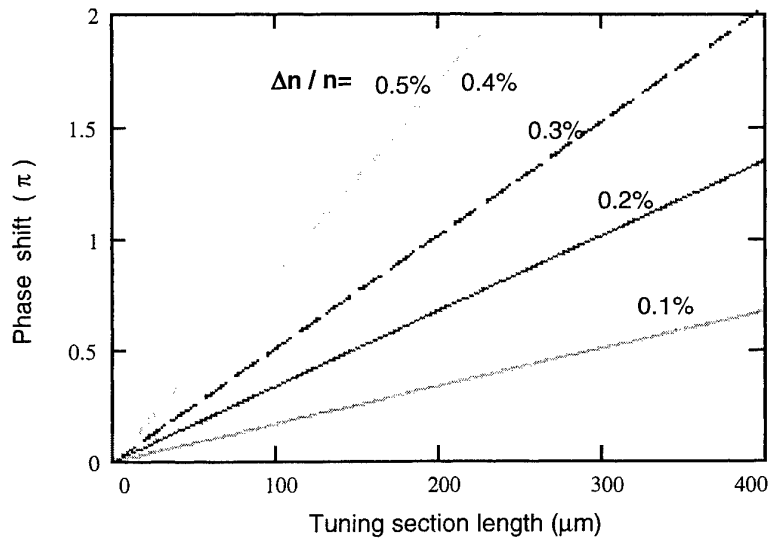


Fig.1.21 Phase shift versus tuning section length due to QCSE, with relative refractive index change as parameter.

Thus a tuning section length of $300\mu\text{m}$ should be adequate to give tuning through a Fabry-Perot mode space.

Concerning the dynamic tuning performance where high frequency modulation is desired, the parasitic parameters are going to be important. It is therefore useful to estimate their effect. Fig.1.22 is the schematic diagram with parasitic capacitance appearing in the tuning section due to semiconductor junction C_j .

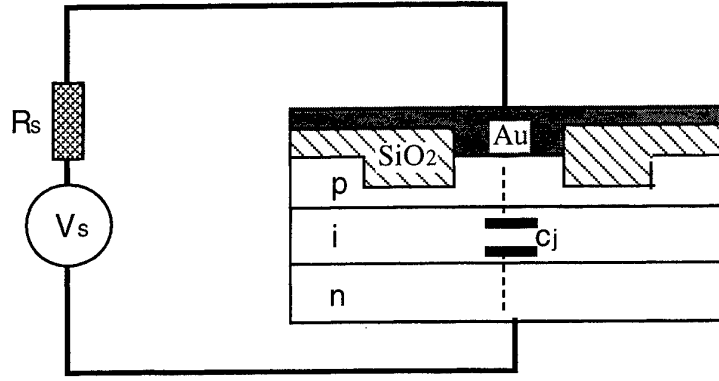


Fig.1.22 The schematic diagram shows the parasitic capacitance of the tuning section.

The junction capacitance can be written as

$$C_j = \epsilon_{r(\text{GaAs})} \epsilon_0 \frac{A_j}{w_d}$$

where A_j is the junction area and w_d the junction depletion region width. For a $250\mu\text{m}$ wide, $300\mu\text{m}$ long cavity ridge waveguide device, ϵ_r is 13.1, $A_j = 250\mu\text{m} \times 300\mu\text{m}$, $w_d \approx 0.3\mu\text{m}$, giving $C_j \approx 29\text{pF}$. If the modulation source internal resistance $R_s = 50\Omega$, the frequency response cut-off frequency f_0 is then

$$f_0 = \frac{1}{2\pi R_s C_j} \approx 100 \text{ MHz}$$

This is a serious limitation to the high frequency perform assessment. It is seen the limitation is mainly due to the junction capacitance in which the large junction area is the main reason. This is because in order to have a proper waveguide, trench etching can only go down above the core layer within the p-AlGaAs cladding layer, rather than go down through the whole i-region as show in Fig.1.22. In an actual device, the etched trench and the ridge metal contact reduces the effective junction area. Depending on the current lateral spreading, C_j should be smaller than that calculated here due to the effective junction area shrinking. A 22pF capacitance in the tuning section is measured for a 2-section laser with 1V reverse bias on the tuning section. It is still very large. Due to this parasitic parameter limitation, it is difficult to actually evaluate the tuning performance beyond the cut-off frequency. It is therefore necessary to reduce this parasitic capacitance in order to test the tuning dynamically. One way to do this is to further etching down through the whole i-region at a location beyond the trench to reduce the junction area, this is the so-called mesa etched laser^{21,22}. If the junction area is reduced to $20\mu\text{m}$ in width, the cut-off frequency will be increased to $\sim 1.4\text{GHz}$ in the case that junction capacitance is the only source of the parasitic capacitance. To fabricate a mesa etched laser, some modifications to the

current design are needed, and the air bridge technique^{23,24} may be also needed to eliminate dielectric capacitance for the new design. As is seen above, when C_j is other parasitics become important. This is discussed in Chapter 4.

References

1. L. M. Magid, *Electromagnetic fields, Energy, and waves*, Chap.9. New York: John Wiley&Sons,1972
2. H. Kressel and J. K. Butler, *Semiconductor lasers and Heterojunction LEDs*. New York: Academic Press, 1977
3. G. H. B. Thompson, *Physics of Semiconductor Laser Devices*. Chichester: John Wiley&Sons, 1980
4. T. H. Zachos and J. E. Ripper, *IEEE J. Quantum Electr.*, **QE-5**, 29(1969)
5. T. Tsukada, *J. Appl. Phys.*, **45**, 4899(1974)
6. W. T. Tsang and R. A. Logan, *Appl. Phys. Lett.*, **45**, 330(1984)
7. J. Buus, *IEEE J. Quantum Electr.*, **QE-18**, 1083(1982)
8. A. Taflove, " Review of the formulation and applications of the finite-difference time-domain method for numerical modeling of electromagnetic wave interactions with arbitrary structures", *Wave Motion*, **10**, 547-82(1988)
9. R. E. Smith, L. A. Molter and M. Dutta, "Evaluation of refractive index approximations used for mode determination in MQW slab waveguides", *IEEE J. Quantum Electr.*, **27**(5), 1119-22 (1991)
10. Rahman_BMA, Liu_Y, Grattan_KTV, "Finite-element modeling of one- and two-dimensional MQW semiconductor optical waveguides", *IEEE Photonics Tech. Lett.*, **5**(8), 928-31(1993)
11. *EMIS Dateviews Series No. 2*, " Properties of GaAs", INSPEC, Section 8.7, (1986)
12. *EMIS Dateviews Series No. 7*, " Properties of AlGaAs", edited by S. Adachi, INSPEC, Section 5.5, (1993)
13. P. C. Kendall, M. S. Stern and S. V. Burke, "Planar waveguide analysis by spectral index method. I: Rib and uniformly buried waveguides", *Optical and Quantum Electronics*, **25**, 771-787 (1993)
14. S. V. Burke, " Planar waveguide analysis by spectral index method. II: Multiple layers, optical gain and loss", *Optical and Quantum Electronics*, **26**, 63-77 (1994)
15. D. Marcuse, *Theory of Dielectric Optical Waveguide*. New York: Academic Press, 1991
16. P. M. Morse and H. Feshbach, *Methods of Theoretical Physics*, Chapt. 9. New York: McGraw-Hill Book Company, 1953

17. D. Marcuse, *Light Transmission Optics*. New York: Van Nostrand Reinhold Co., 1982
18. J. J. Lepore, "An improved technique for selective etching of GaAs and AlGaAs", *J. Appl. Phys.*, **51**, 6441-2(1980)
19. K. Hikosaka, T. Mimura and K. Joshin, "Selective dry etching of AlGaAs-GaAs heterojunction", *Jpn. J. Appl. Phys.*, **20**, L847-50(1981)
20. F. Stern, *J. Appl. Phys.*, **47**, 5382(1976)
21. Lester_LF, Schaff_WJ, Offsey_SD, Eastman_LF, "High-speed modulation of InGaAs-GaAs strained-layer multiple-quantum-well lasers fabricated by chemically assisted ion-beam etching", *IEEE Photonics Techn. Lett.*, **3**(5), 403-5(1991)
22. Weisser_S, Ralston_JD, Larkins_EC, Esquivias_I, Tasker_PJ, "Efficient high-speed direct modulation in p-doped In_{0.35}Ga_{0.65}As/GaAs multiple quantum well lasers", *Electronics Lett.*, **28**(23), 2141-3(1992)
23. Delage_SL, Blanck_H, Chartier_E, Cassette_S, Floriot_D, Perreal_Y, Pons_D, Roux_P, Bourne_P and Chaumas_P, "GaInP/GaAs heterojunction bipolar transistor. Technology and microwave performances", *Revue Technique Thomson - CSF*, **26**(2), 367-402(1994)
24. Hirano_M, Imai_Y, Toyoda_I, Nishikawa_K, Tokumitsu_M, Asai_K, "Three-dimensional passive elements for compact GaAs MMICs", *IEICE Transactions on Electronics*, **E76-C**(6), 961-7(1993)

Chapter 2. Device Fabrication Progress

Because of the success in fabricating the CW laser in first year, we are able to concentrate on further development of the technology toward operating GaAs/AlGaAs MQW the final device desired. The main progress achieved since last year could be summarised as follows.

In our early devices, Cr/Au was used as an Ohmic-contact metal to the p-GaAs cap layer, which we found presented large contact resistance. The resistance was so large that it limited the deliverable power output to below 10 mW. In order to solve this problem, the Zn/Au p-contact metal system was developed. This is discussed in Section 2.1.

For ridge waveguide devices, wet chemical etch is normally used for trench etch, due to its convenience and controllability. The widely used etchants are H_2SO_4 , H_3PO_4 and NH_4OH based etching systems, which all tend to give a non-uniform, non-flat, and non-mirror etched surface. The uniformity is so bad that the actual etched depth varies from 0.61 to 1.34 μm in the same etched wafer (roughly 1 by 1.5 cm^2) for a nominal etch depth 1.2 μm . We develop a new etchant to tackle the problem. This is dealt with in section 2.2.

Indium is used as an eutectic solder for laser die bonding because of its low application temperature. However, serious problems were found due to its bad wetting, bad sticking, high thermal resistance and unreliability, therefore, Sn/Au is introduced to substitute for indium as the eutectic solder for laser die bonding. This is reported in 2.3

Many experiments have been run on ion implanted two section lasers. In 2.4, detailed processing and experiments on H^+ and O^+ implanted samples are reported. Successful 2-section lasers with good isolation fabricated by H^+ implantation are also reported.

Band gap shifting in the tuning section is necessary to achieve low loss, pure field tuning laser. Experiments with SrF_2 and SiO_2 capped annealing, using the effect of impurity-free vacancy diffusion (IFVD), have been carried out, and promising results have been obtained although problems are found with SrF_2 . Further work using new dielectric films instead of SrF_2 is planned. This is introduced in 2.5.

Most problems concerning the fabrication of a good quality laser have been overcome during the year and substantial progress in using ion implantation to achieve completely isolated 2-section lasers and using IFVD to achieve band gap shifted 2-section lasers has been made.

2.1. Ohmic contact on p-GaAs improvement

We used to use Cr/Au as the p-GaAs Ohmic contact metal which has very good adhesion, but its contact resistance is too big to be ideal for laser diodes. Due to the large contact resistance, thermal heating effects prevent large optical power output as once pumping level increased, the heat produced burns out the laser very quickly, and in our early devices, the maximum CW output power never exceeded 10mW, even for a short time. Another effect is the degradation of threshold current is rapid. This problem was identified in our first year report (Section 4.1, p55; first year report), and an effort has been made since then to overcome it.

Zn/Au provides a good Ohmic contact to p-GaAs, but people are cautious in using it because of its high contamination due to its high diffusion ability, it is also possible to contaminate the vacuum system if it is not used properly. Another problem is the poor adhesion of Zn to GaAs making the bonding to the electrode pad very tricky. Due to the good adhesion of Au on GaAs, and the low eutectic temperature($\sim 390^\circ\text{C}$ depending on composition) of Au/Zn alloy, we explored using Au/Zn/Au instead of Zn/Au as the new contact metal. Very low contact resistance as well as very good adhesion on p-GaAs are achieved, as shown in Fig.2.1, the specific resistance is improved from $2 \times 10^{-4} \Omega\cdot\text{cm}^2$ for Cr/Au to about $1.5 \times 10^{-5} \Omega\cdot\text{cm}^2$ for Au/Zn/Au, better than an order of magnitude improvement in specific contact resistance. For a normal $600\ \mu\text{m}$ laser, this means the

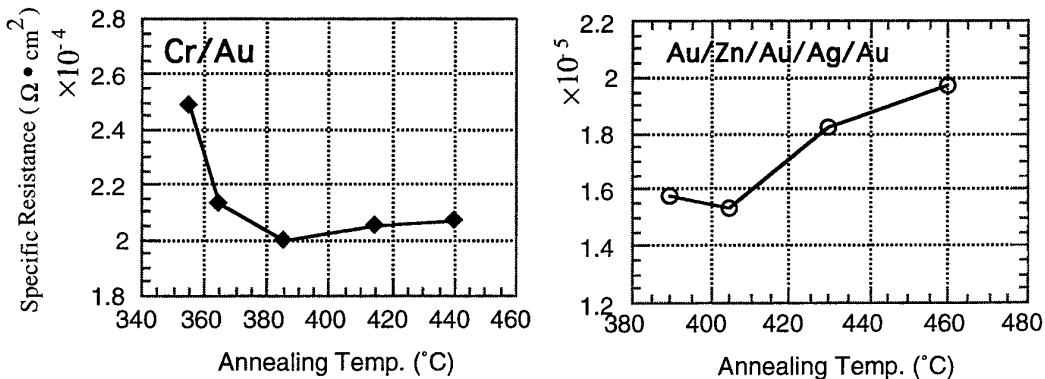


Fig.2.1 Specific contact resistance variation with annealing temperature for Cr/Au and Au/Zn/Au contact metal to p-GaAs.

contact resistance is reduced from 11Ω to less than 1Ω . The key technique here is very thin Au(about 5 nm) deposition first followed by proper Zn deposition ($\sim 15\ \text{nm}$), and

then normal Au for correct composition alloy (~40nm), followed by diffusion barrier metal (Ag) and final covering metal (Au). Together with consistent wafer treatment processing before deposition and thermal annealing (~400°C, 1 minute) after the evaporation, the Au/Zn/Au/Ag/Au p-contact system works reliably with no special care needed. More importantly, much better laser performance is achieved: for a typical laser using this contact metal, power in excess of 20 mw is easily achievable, Fig.2.2 is a typical result; enormous improvement in the threshold degradation is found. Although

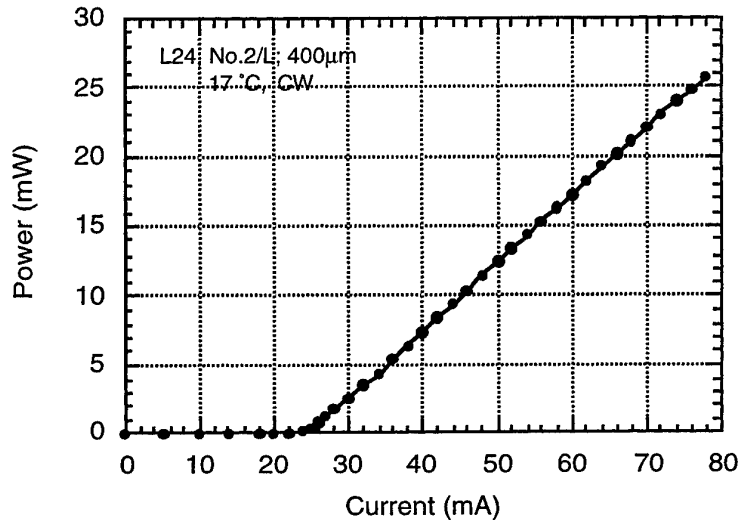


Fig.2.2 A typical L-I plot for laser fabricated by Au/Zn/Au contact. The average slope efficiency in this plot is 0.48 mW/mA/facet.

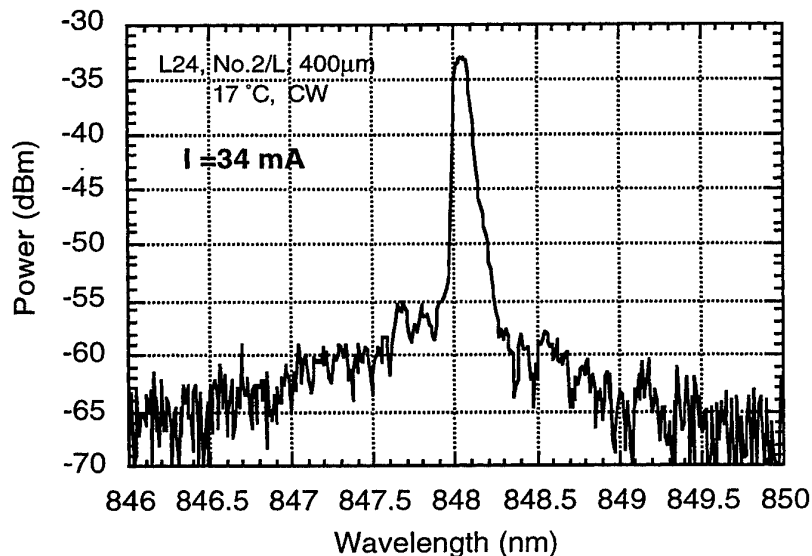


Fig.2.3 A typical spectrum plot for laser fabricated by Au/Zn/Au contact. The MSR in this plot is 22 dB.

a formal ageing test has not been performed, in a day-to-day base experiment running, threshold current is quite stable for at least one week which is good enough for any test.

The slope efficiency is also improved from below 0.15 mW/mA/facet to an average 0.4 mW/mA/facet, and the highest ~0.55 mW/mA/facet. Due to the output power improvement, mode suppression ratio (MSR) is also improved¹ as shown in Fig.2.3.

2.2 Chemical wet etch in defining ridge

As modelled in Chapter 1, the ridge height is a critical factor in deciding laser mode and threshold condition. Multiple lateral modes consume energy to reduce the power from the main mode, resulting in bad MSR. Precisely control of the etch depth therefore become very important.

Etching GaAs/AlGaAs is a very well developed process nowadays, which can be classified as dry etch^{2,3} and wet etch⁴⁻⁶. Dry etch normally requires a vacuum system, while it can give a flat etched surface, very good uniformity over the whole wafer, its controllability on etch depth is always very bad, therefore, several runs of this etch process are often needed in order to produce the depth required. This is a very time-consuming and energy wasting process. Although we also used dry etch in our early device processing, we finally decided to search for more applicable wet chemical etch process.

Wet etch has very good controllability: the etch speed is controllable by using different etchant, or different concentration; etch depth can be controled conveniently by frequently measuring the depth etched. The only problems are with the etched surface quality and uniformity of etch depth. By using the most widely used etchants based on H_2SO_4 , H_3PO_4 and NH_4OH , with different concentrations, we studied the etched surface and uniformity after etch. The uniformity is defined as

$$\Delta d = \frac{d_{\max} - d_{\min}}{d_{\text{ava}}}$$

where d_{\max} is the depth maximum measured, d_{\min} the minimum in the same wafer and d_{ava} the average depth accounted. Table 2.1 summarises the results.

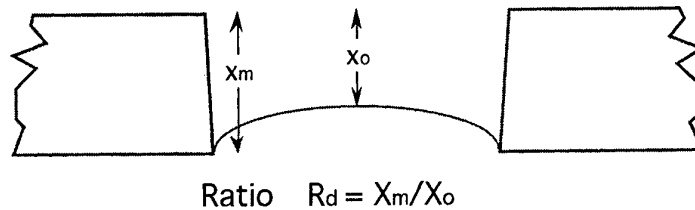



Fig.2.4 Normal profile after etch by H_2SO_4 , H_3PO_4 or NH_4OH based etchant.

The profile after etch is normally that displayed in Fig.2.4, with different value of R_d , but in any case, $R_d > 1$ is always obtained. This can be understood from the fundamental mechanism the GaAs wet etch involved.

Table 2.1 Etching experiments summary

Etchants	d_{\max}	d_{\min}	d_{ave}	Δd	Etched surface
$\text{H}_2\text{SO}_4 : \text{H}_2\text{O}_2 : \text{H}_2\text{O}$ 1:8:60	1.34	0.61	1.21	60%	rough/texture surface, $R_d=1.18$ 
$\text{H}_2\text{SO}_4 : \text{H}_2\text{O}_2 : \text{H}_2\text{O}$ 1:1:30	1.28	0.97	1.2	26%	rough/texture surface, $R_d=1.21$
$\text{H}_2\text{SO}_4 : \text{H}_2\text{O}_2 : \text{H}_2\text{O}$ 4:1:1	1.36	1.25	1.3	8.5%	rough/texture surface, $R_d=1.24$
$\text{H}_3\text{PO}_4 : \text{H}_2\text{O}_2 : \text{H}_2\text{O}$ 1:2:20	1.38	0.68	1.23	57%	rough/texture surface, $R_d=1.14$
$\text{H}_3\text{PO}_4 : \text{H}_2\text{O}_2 : \text{H}_2\text{O}$ 1:1:30	1.42	1.15	1.21	22%	rough/texture surface, $R_d=1.1$
$\text{H}_3\text{PO}_4 : \text{H}_2\text{O}_2 : \text{H}_2\text{O}$ 3:1:50	1.27	1.16	1.25	9%	rough/texture surface, $R_d=1.17$
$\text{NH}_4\text{OH} : \text{H}_2\text{O}_2 : \text{H}_2\text{O}$ 1:1:20	1.44	1.21	1.3	18%	shining surface, $R_d=1.2$
$\text{NH}_4\text{OH} : \text{H}_2\text{O}_2 : \text{H}_2\text{O}$ 3:2:50	1.35	1.1	1.27	20%	shining surface, $R_d=1.15$
$\text{NH}_4\text{OH} : \text{H}_2\text{O}_2 : \text{H}_2\text{O}$ 3:1:50	1.42	1.21	1.34	16%	shining surface, $R_d=1.17$

Most etchant for GaAs contain an oxidising agent such as H_2O_2 , a complexing agent such as H_2SO_4 and dilutant such as water. The etch process starts when oxidising towards GaAs surface by diffusion. The active site of the GaAs adsorbs H_2O_2 , and an oxide of GaAs is formed. Further H_2O_2 , or its decomposed product such as an oxygen ion will reach the oxide-GaAs interface through the wholly or partially oxidised GaAs surface layer by diffusion, to further react with GaAs. Although the oxidised layer is normally insoluble in water, the complexing agent reacts with this layer very well and forms a soluble complex to dissolve into water. The resultant etched surface totally depends on the relative reaction rate between oxidising and complexing. If the oxidising rate is faster than the complexing rate, the etch become reaction-rate-limited. If it is the reverse, the etch become diffusion-limited as in this case it is the oxidiser diffusion rate

which limits the reaction. Etchants containing high concentrations of complexing agent but low concentrations of oxidiser are usually diffusion limited, otherwise, it is reaction-rate-limited. Thus by changing the concentration of complexer and oxidiser, an etchant could be either diffusion or reaction-rate limited.


For the masked GaAs surface, at the edge of opened window, the availability of fresh, unreacted etchant from the nearby masked area causes abnormally high etch rate within the window near the edge. This is the mask edge trenching effect shown in Fig.2.4. A flat etched bottom can only be seen at a distance as much as 50~300 μm away from the edge, but the trench of our device is only 10 μm in width. For reaction-rate-limited etchant, local oxide defect (which normally is very high) will result in a rough surface. Furthermore, the oxidation is very sensitive to the surface bonds and states, but normally an epitaxial wafer tends to be non-uniform in its surface bond activity or surface states after growth, resulting in very non-uniform oxidising in the same wafer, giving bad etch depth uniformity. For our application, this is the case we should avoid. Diffusion-limited etchant is needed.

Unfortunately, H_2SO_4 , H_3PO_4 and NH_4OH based etchants all have high reaction rate with GaAs, resulting in serious mask edge trenching effect as listed in Table 2.1. Even if there is no H_2O_2 , H_2SO_4 or H_3PO_4 solution is still reactive with GaAs, therefore, trenching effect always inevitable. On the other hand, high concentration H_2SO_4 or NH_4OH etchant damages the photoresist mask quickly, resulting in a badly defined ridge. The best solution is to find a weak acid with low reactive rate to GaAs, to form a diffusion limited etchant. This is mainly because only very low reaction rate, 'gentle' acid will help to produce a flat etched profile and a mirror etched surface since only low etch rate will reduce the etch rate difference between the centre and the edge area.

Citric acid⁷ is a very suitable candidate for our purpose. It is a weak acid with slow etch rate on GaAs, no attack on resist at all. By using citric acid/ H_2O_2 / H_2O etchant, we always have obtained very good flat bottom with shining/mirror etched surface and very good uniformity, as listed in Table 2.2. The only problem is that citric acid seems to be a selective etchant which stops at the interface of GaAs/AlGaAs when Al composition is high enough. We therefore modify the etchant by adding a little H_3PO_4 which we believe will etch AlGaAs very well. Indeed, with the assistance of very low concentration H_3PO_4 , the etchant works very well for Al composition from 0.2~0.6, which is the sample range we have. In fact, this etchant has a wide range of tolerance: with the ratio citric acid: H_2O_2 : H_2O : H_3P_4 = 50:2~8:50:1~3, the results always show a

very flat bottom, mirror surface and very good uniformity which fulfil the requirement for our ridge waveguide laser completely.

Table 2.2. Ridge define etching by citric acid based etchant.

Etchants	d_{\max}	d_{\min}	d_{ave}	Δd	Etched surface
citric: H_2O_2 : H_2O 50:4:50	1.19	1.21	1.2	2%	mirror surface, $R_d=1.0$, stop at AlGaAs 
citric: H_2O_2 : H_2O 60:10:60	1.61	1.55	1.6	3.6%	mirror surface, $R_d=1.03$, stop at AlGaAs
citric: H_2O_2 : H_2O : H_3PO_4 15:5:15:1	3.99	3.83	3.94	4%	mirror surface, $R_d=1.07$, etch AlGaAs
citric: H_2O_2 : H_2O : H_3PO_4 30:2:30:1	1.59	1.55	1.58	2.5%	mirror surface, $R_d=1.02$, etch AlGaAs

2.3 Improvements in laser die bonding

After laser cleaving and separating, the laser die is mounted on to a heat sink by eutectic metal bonding. In our early lasers, Indium was used as the eutectic solder to bond the laser die on a brass base, Au plated mount. Flux is used to improve the wetting property of In/Au, where Au is on both heat sink and the laser die surfaces. Soon very serious problems were found in using the In solder: firstly, the wetting property is very bad indeed. Although In melts at very low temperature (156 °C), it does not wet Au surface at all. Flux certainly helps to improving the wetting property to some extent, but the flux coats not only the bottom of the die, but also the side and top of it, therefore, giving In the chance of going to the top and side of the die as well, resulting the failure of the device. Secondly, due to the bad wetting, In is not spread on the bonding surface uniformly. Holes or channels appear between the In/die and In/heat sink surface, resulting in a high thermal resistance. Lastly, as In is a soft metal with bad wetting, it does not stick the die very well. During ultrasonic wire bonding, even the small bonding force shakes the die and resulting an unreliable die/In contact. The result is In bonding become an important possible factor in accelerating the degradation of the laser performance. Indeed, other researchers⁸ reported that the thermal resistance and threshold increase of In bonded devices far exceeded that for devices bonded by SnAu or GeAu eutectic alloy (150 and 3.6 times, respectively) during ageing tests.

SnAu (20% Sn, 80%Au) and GeAu (12% Ge, 88%Au) are widely used eutectic alloys in commercial laser bonding, their melting temperature is 280 and 356 °C, respectively. 356°C is a high temperature for manual operation and therefore, not convenient for us. SnAu alloy is the best candidate for our purpose. After experiment, the advantages of SnAu alloy become obvious: the wetting property is very good, it automatically wets any surface with Au coating, therefore, no flux is needed, which guarantees a clean device; the bonding performance is also excellent, no device was found to be loose during ultrasonic wire bonding since using SnAu. More importantly, the stable working life time (before threshold current increasing dramatically) is found increased from several days for the In bonded laser to at least two weeks for the SnAu bonded laser.

2.4. Ion implantation processing

Ion implantation is used to create an electrically non-conductive region between the gain and the tuning section to enable a reverse bias to be applied to the tuning section. Two atoms, hydrogen and oxygen are selected as ions to create H^+ or O^+ implanted isolation area. Several runs of implantation have been performed for O^+ and H^+ , respectively. The processing details and results are reported as follows.

2.4.1. O^+ implantation

Oxygen is a specimen who creates the high resistivity region not only by ion-created defects, but also by chemical doping effect^{9,10}, therefore, O^+ implantation has much higher carrier trapping efficiency than H^+ implantation⁹. Moreover, it is found that even implanted defects are annealed out by thermal annealing, the oxygen doping effect still keeps the resistivity of O^+ implanted region very high. This is attractive to us in the sense that if O^+ is implanted into the active region, we need the defect to be annealed out, but we need the region to be still of high resistivity. Table 2.3 shows the results we have obtained so far on the O^+ implanted samples. O^+ is implanted into the isolation region shown as in Fig.1.1. In the table, 1-section means the laser comes from the same wafer but has only one section with no O^+ implanted region, and 2-section means there is a O^+ implanted region between the gain and the tuning sections. Sample TL104, which is from QT787R, has a multi-energy high dose implantation which creates a projection depth of 1.5 μ m, with optimised annealing temperature for high resistance, therefore very high isolation resistance is obtained; but because the high defect density is not annealed out, high loss due to the non-radiative recombination process occurs in this region, resulting in a threshold condition too high to be reached. Sample TL112, which is from QT862, was implanted with lower energy and doses with the projection

depth of only $1\mu\text{m}$. A series of annealing temperatures was used to investigate the isolation resistance, as plotted in Fig.2.5. When there is no annealing or the annealing temperature is low, typical hopping conductivity⁹ is seen to produce low isolation resistance; when sample is annealed within $500\sim 700^\circ\text{C}$, isolation resistance increases to maximum, and then falls quickly with further increase in annealing temperature.

Table 2.3 O⁺ implantation process and results

Sample	Implantation Energy	O ⁺ dosage (cm ⁻²)	Anneal	Isolation resistance	Device performance
TL104	1MeV	3×10^{14}	RTA 600°C 15 sec.	$>700\text{M}\Omega$	1-section: laser 2-section: LED
	500KeV	3.3×10^{14}			
	200KeV	2.4×10^{14}			
	100KeV	9×10^{13}			
	50 KeV	6×10^{13}			
TL112	500KeV	1×10^{14}	see text	see text	1-section: LED 2-section: LED
	150KeV	1×10^{14}			
	50 KeV	9×10^{13}			
TL111	1MeV	1×10^{14}	RTA 900°C 15 sec.	$\sim 5\text{K}\Omega$	1-section: laser 2-section: bad laser ($I_{\text{th}} \sim 80\text{ mA}$)
	70 KeV	7×10^{13}			

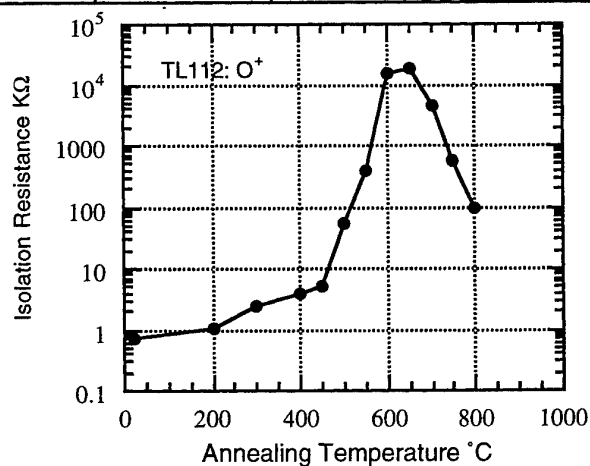


Fig.2.5 Isolation resistance varies with annealing temperature for sample TL112.

Unfortunately, this sample did not lase, even for a single section device. The reason for this is not because of the ion implantation, but because of quality of wafer. From the same wafer we fabricated stripe lasers and ridge waveguide lasers with both having no ion implantation, both sets of devices failed to lase also.

In TL111 (from QT787), the top p^+ -GaAs contact layer is removed by selective etch in the isolation region. The sample is implanted with only two energies: 1MeV is used to create isolation deep down to the active layer (1.5 μ m projection depth which covers the whole MQW active thickness) and low energy is used for isolating the top layers. After implantation, the wafer is coated with SiO₂ above one section, and SrF₂ above another section in order to produce quantum well band gap shifting while doing the annealing for implantation. After the relatively higher temperature annealing, isolation resistance is not very high, and the problems associated with SrF₂ capped annealing is found. The details will be discussed in the next section, however the result of cutting the SiO₂ capped and annealed section into a 1-section device is a laser with $I_{th} \sim 25$ mA; if a 2-section device is made with one section SiO₂ capped and another section SrF₂ capped, and pumping the SiO₂ capped section, the device can lase, but with an extremely high threshold current (~ 80 mA), which is the result of SrF₂ capped section acts as a high loss absorber; if the SrF₂ section is pumped, or even a 1-section device cut from SrF₂ capped section is pumped, the device not only can not lase, but also the emitted light is too weak to be a LED.

In conclusion, O⁺ implantation creates very high isolation resistance between the two sections if annealing temperature is in the optimised range 550~700°C. High temperature annealing can remove the defect penetrated into the active layer to enable device lasing. It is possible to find a suitable dose and annealing temperature to make the device lase while keeping a high isolation resistance. To perform band gap shift annealing and implantation annealing together is not a good scheme as the optimised temperatures for each are not the same.

2.4.2 H⁺ implantation

H⁺ implantation creates carrier trapping defects to form a high resistivity region^{9,11}. Due to the low atomic diameter of hydrogen, only low energy implantation is needed for a relative deep penetration. For H⁺, unlike O⁺, only the implanting defects produce high resistivity, therefore H⁺ is not so effective as O⁺ in producing good isolation⁹. The advantage of H⁺ is its low annealing temperature: 200~420 °C is the optimised annealing temperature for best resistivity which could be done while performing metalisation annealing. Table 2.4 shows the results of H⁺ implantation in our device.

From the results it is seen quite clearly that high dose and high implantation energy (TL106 from QT703R, with projection depth of 1.7 μ m), although producing a high resistance region, the high optical loss within this region in the active layer prevents the

device lasing. On the other hand, low dose, low implantation energy (TL108, TL109 from QT787 with projection depth of 1.2 μm) do not stop the device from lasing, but the isolation resistance is poor. Only intermediate implantation energy and dose, as in sample TL111B (from QT787 with projection depth of 1.5 μm), keep the device lasing while maintaining a moderate isolation resistance. TL111B is a successful sample with very high yield of two section lasers. Fig.2.6 is a typical light power and tuning section current leakage plot with gain section pumping current. Detailed device performance will be discussed in the next chapter.

Table 2.4. H⁺ implantation processing and results.

Sample	Implantation Energy	H ⁺ dosage (cm ⁻²)	Anneal	Isolation resistance	Device performance
TL106	230KeV	4x10 ¹⁴	395°C	~ 100M Ω	1-section: laser
	200KeV	3x10 ¹⁴	2 min		2-section: LED
	150KeV	4.3x10 ¹⁴			
	100KeV	3.5x10 ¹⁴			
	50 KeV	3x10 ¹⁴			
TL108	150KeV	4.3x10 ¹²	380 °C	~ 100 Ω	1-section: laser
	100KeV	3.5x10 ¹²	30 sec		2-section: laser
	50 KeV	3x10 ¹²			
TL109	150KeV	4.3x10 ¹³	390 °C	~ 400 Ω	1-section: laser
	100KeV	3.5x10 ¹³	1 min		2-section: laser
	50 KeV	3x10 ¹³			
TL111B	200KeV	8x10 ¹³	400 °C	~ 20 K Ω	1-section: laser
	150KeV	6x10 ¹³	30 sec		2-section: laser
	100KeV	9x10 ¹³			
	50 KeV	7x10 ¹³			

For hydrogen implantation, one concern remains. This is the high diffusion and instability of hydrogen⁹. Due to its high activity, H is not stable in semiconductors. In our device, we observed the slope efficiency decreasing in a H⁺ implanted stripe laser

having the same dose and energy as TL109 relative to unimplanted lasers fabricated from the same wafer. The slope efficiencies were 0.27 and 0.4 W/A, respectively. The ion energy used is not high enough to make H^+ reach active layer of the laser, but during annealing, the hydrogen is driven into the active layer. The resulting H doping forms non-radiative recombination centre in this layer and decreases the radiative emission efficiency. For a stripe geometry laser, this effect is more pronounced than for a ridge waveguide laser.

In conclusion, proper H^+ implantation dose and energy has been researched and a run of successful H^+ implanted 2-section lasers, with good isolation between sections has been achieved. Further investigation is needed for the life time problem, stability problem and whether it is possible to implant H^+ with a proper dose to reach the active layer.

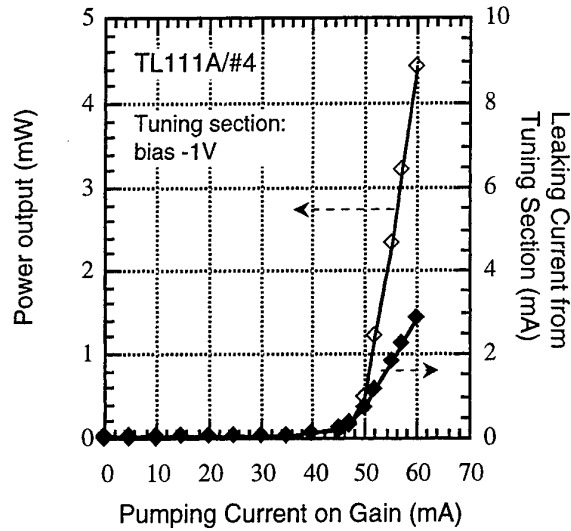


Fig.2.6 H^+ implantation isolated 2-section laser from TL111A. Power output and -1V biased tuning section leaking current plot while pumping the gain section.

2.5. Band gap shifting processing

In order to make the tuning section work in a very low absorption region while still displaying QCSE, the band gap of the MQW in the tuning section needs to be increased (exciton edge blue shifted), while keeping the MQW in the gain section unchanged. If this is achieved, the lasing wavelength will be in the low absorption red side of the exciton edge of the tuning section.

As described in the first year report, impurity free vacancy diffusion (IFVD) is the technique we propose to achieve this purpose. By using different dielectric capping films above tuning and gain sections, and annealing the sample at about 900 °C, the band gap of MQW beneath them will be widened to different extents, and MQW relative band gap shifting is performed^{13,14}. The best dielectric to produce large shifting is SiO_2 , and the dielectric film that best protects MQW from band gap shifting is SrF_2 .

First, PECVD SiO_2 is deposited over the whole wafer, then by photolithography, SiO_2 is removed from the area needing to be protected from shifting. SrF_2 is then deposited by thermal evaporation over the wafer. Finally the wafer is annealed by rapid thermal annealing (RTA) equipment at 900°C for 15 seconds. As described in the last section, sample TL111 was fabricated including this process.

Serious problems were found associated with applying SrF_2 . After annealing and removing SrF_2 , serious residual product was found at the SrF_2 site, which we confirmed to be some kind of product of GaAs and SrF_2 reaction at high temperature. This by-product can not be removed by cleaning, except by etching the whole area. After metallisation and cleaving, devices made from this portion only emitted weak light, even with very hard current pumping. The reason for this is not clear yet, but other groups who use the same technique have observed similar problems¹⁴. Although theoretically SrF_2 is an inert compound, it is possible for it to be reactive under high temperature.

Despite the problems in laser fabrication, obvious MQW band gap tuning is still achieved. Fig.2.7 is the PL spectra comparison between SiO_2 and SrF_2 capped areas. As large as 17 nm exciton peak shift is achieved. Lasers made from SiO_2 capped portion have the lasing wavelength ~ 830.5 nm, but the lasers made from the same wafer with no cap annealing performed have a lasing wavelength ~ 842 nm, confirmed the obvious band gap shifting of the MQW.

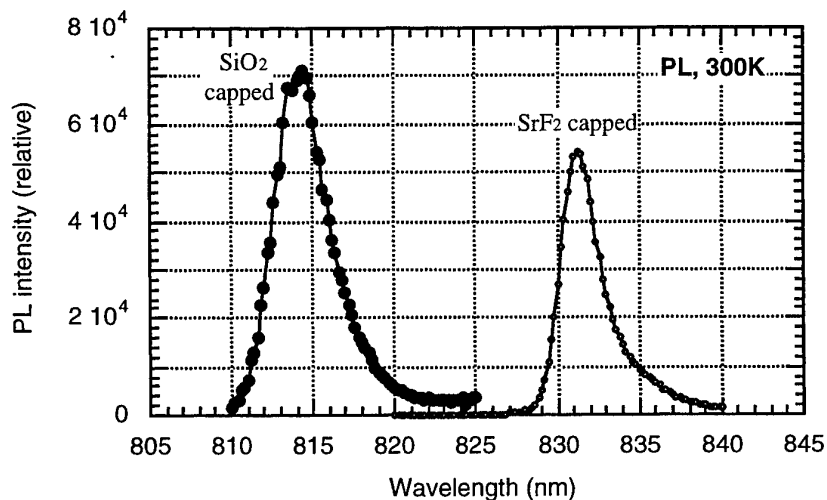


Fig.2.7 PL spectra of SiO_2 and SrF_2 capped samples annealing at 900°C for 15 sec. The MQW exciton peak shows a relative difference of $\sim 17\text{nm}$ after annealing.

A new dielectric film, $\text{SiO}_2\text{:P}$, is already under investigation to substitute SrF_2 as the protecting film¹⁵. In the sense that $\text{SiO}_2\text{:P}$ has the similar physical and chemical properties to pure SiO_2 , this film, as used by another group, offers better prospects for laser fabrication than SrF_2 .

References

1. T. P. Lee, C. A. Burrus, J. A. Copeland, A. G. Dentai and D. Marcuse, *IEEE J. Quantum Electron.*, **OE-18**, 1101(1982)
2. R. E. Lee, "Minifabrication by ion beam etching", *J. Vac. Sci. Technol.*, **16**, 164-70(1979)
3. R. A. Powell, "Reactive ion beam etching of GaAs in CCl_4 ", *Jap. J. Appl. Phys.*, **21**, L170-2(1982)
4. D. J. Stirland and B. W. Straughan, "A review of etching and defect characterisation of GaAs substrate material", *Thin Solid Films*, **31**, 139-70(1976)
5. Y. Mori and N. Watanabe, "A new etching solution system, $\text{H}_3\text{PO}_4\text{-H}_2\text{O}_2\text{-H}_2\text{O}$, for GaAs and its kinetics", *J. Electrochem. Soc.*, **125**, 1510-14(1978)
6. S. Iida and K. Ito, "Selective etching of GaAs crystals in $\text{H}_2\text{SO}_4\text{-H}_2\text{O}_2\text{-H}_2\text{O}$ system", *J. Electrochem. Soc.*, **118**, 768-71(1971)
7. M. Otsubo, T. Oda, H. Kumabe and H. Miiki, "Preferential etching of GaAs through photoresist masks", *J. Electrochem. Soc.*, **123**, 676-80(1976)
8. K. Fujiwara, T. Fujiwara, K. Hori and M. Takusagawa, "Aging characteristics of GaAs double-heterostructure lasers bonded with gold eutectic alloy solder", *Appl. Phys. Lett.*, **34**(10), 668-670(1979)
9. S. J. Pearton, "Ion implantation in III-V semiconductor technology", *Int. J. Modern Physics B*, **7**(28), 4687-4761(1993).
10. E. V. K. Rao, "Optical properties of oxygen implanted GaAs", *Physica Status Solidi A*, **33**(2), 683-90(1976).
11. P. N. Favannec and D. Diguët, "Electrical properties of proton bombarded GaAlAs", *Appl. Phys. Lett.*, **23**, 546-7(1973).
12. J. C. Dymant, J. C. North and L. A. D'asaro, "Optical properties and electrical properties of proton bombarded p-type GaAs", *J. Appl. Phys.*, **44**, 207-13(1973).
13. I. Gontijo, T. Krauss, J. H. Marsh and R. M. De La Rue, "Post growth control of GaAs/AlGaAs quantum well shapes by impurity-free vacancy diffusion", *IEEE J. Quantum Electron.* **OE-30**(5), 1189-95(1994).
14. J. H. Marsh, "Quantum well intermixing", *Semicon. Sci. & Technol.*, **8**, 1136-55(1993).

15. Hamoudi_A, Rao_EVK, Krauz_P, Ramdane_A, Ougazzaden_A, Robein_D, Thibierge_H, "Controlled disordering of compressively strained InGaAsP multiple quantum wells under SiO:P encapsulant and application to laser-modulator integration", *J. Appl. Phy.*, **78**(9), 5638-5641(1995)

Chapter 3. Device Tuning Performance

Due to the success in fabricating the H^+ implantation isolated 2-section laser, it becomes possible to evaluate the laser tuning performance, including static and dynamic tuning performance. Only after this evaluation can further design and fabrication modification be made properly.

General device characterisation will be discussed first, to give an overview of the device characteristics. This is covered in section 3.1.

Static tuning performance, and the tuning mechanisms observed, are discussed in section 3.2.

The dynamic tuning characterisation method, results and factors restricting the measurement are presented in section 3.3.

3.1. General device characteristics

The device, made from TL111B as discussed in the last chapter, is an H^+ implanted, $400^\circ\text{C}/30$ seconds annealed 2-section CW operating laser. The epitaxial wafer for fabricating this device is QT787 as mentioned in Chapter 1, which is a 4 GaAs quantum well structure. The device is a metal clad ridge waveguide laser, with a ridge width of $5\mu\text{m}$ and nominal rib height $1.2\mu\text{m}$ which was etched by H_3PO_4 based etchant (before the creation of our citric acid based etchant). The peak concentration of H^+ implantation, as modelled by Surrey University, is $2.5 \times 10^{18} \text{ cm}^{-3}$, with a projection range $\sim 1.5 \mu\text{m}$, which is just above the core waveguide layer. Device yield is high ($\sim 90\%$), proving the good quality of the epitaxy and processing. The laser is bonded p-side up by SnAu eutectic alloy on a brass based, Au plated heat sink. No AR or HR coating is applied to the laser facets.

Normal I-V characterisation is performed. It is found the total series resistance (contact, bonding, soldering, wire resistance, etc., plus bulk resistance) is about 8Ω , quite comparable to similar lasers fabricated at Nortel Opto-electronics. The reverse bias break down voltage (at $1 \mu\text{A}$ leakage current) is $7\sim 20 \text{ V}$, which is good enough for our purpose.

For a device with a 300~400 μm long gain section and 200~300 μm tuning section, threshold current is 25~35 mA (lowest ~20 mA) with slope efficiency ~40% at the initial assessment stage. Typical isolation resistance ~20 $\text{K}\Omega$ is normally achievable. Devices with isolation > 100 $\text{K}\Omega$ were also quite common.

Ageing degradation of the two section devices was observed, such as power decreasing with time under constant pumping current, and threshold current increasing on a day-to-day assessment base. Compared to the much more stable CW operation of the single section laser from the same laser chip with the only difference of having no H^+ implanted region in crossing the cavity, it is believed that H^+ implanted defect is migrating during CW lasing, therefore, more and more non-radiative recombination centres are driven into the active layer. The mechanisms for this to be happened could be photon excited defect diffusion^{1,2} or temperature driven diffusion, or both. Although H^+ implantation is widely used in planar stripe lasers and other integrated devices as electrical isolation measure, the degradation of threshold current and quantum efficiency due to the defects induced by H^+ bombardment was reported³ for a stripe laser where the implantation region is along the cavity, and there was no implantation damage inside the optical cavity. As generally realised, H is a high diffusivity, unstable deep level impurity in most semiconductors⁴. Therefore, H^+ is still not a perfect candidate for the isolation purpose.

3.2. Static tuning performance

The assessment diagram is shown in Fig.3.1. The heat sink of the laser is temperature controlled at 20 °C. The coupling efficiency from laser to the single mode fibre is about 25%. The Y coupler divides optical power into 1:9, with 10% power feeding to the power meter.

3.2.1. Optical power output during tuning

During tuning performing measurement, the device is pumped as shown in Fig.3.1. When pumping the gain section above the threshold and varying the reverse bias across the tuning section, measured results show a large variation in optical output power. The output power drops nearly linearly with increasing reverse bias until lasing ceased, as shown in Fig.3.2.

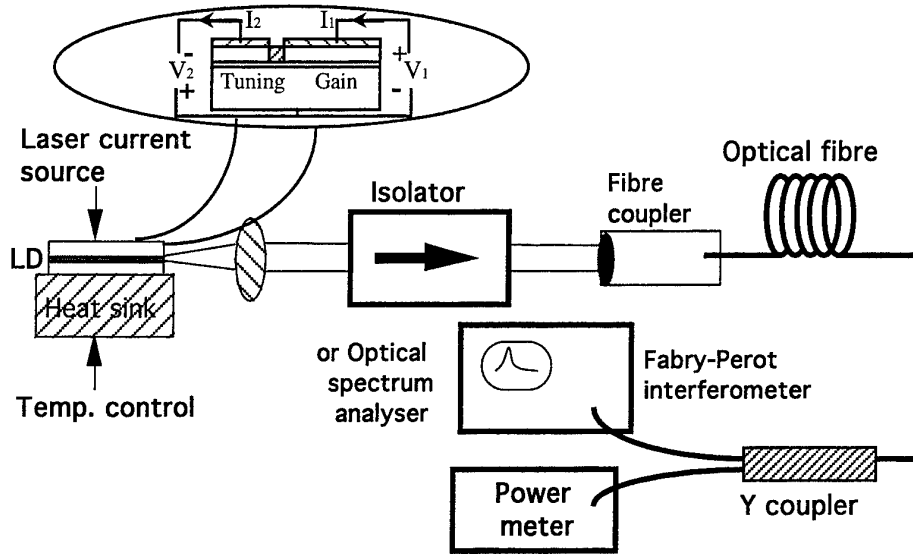


Fig.3.1 Set-up for static tuning performance assessment of 2-section tunable laser.

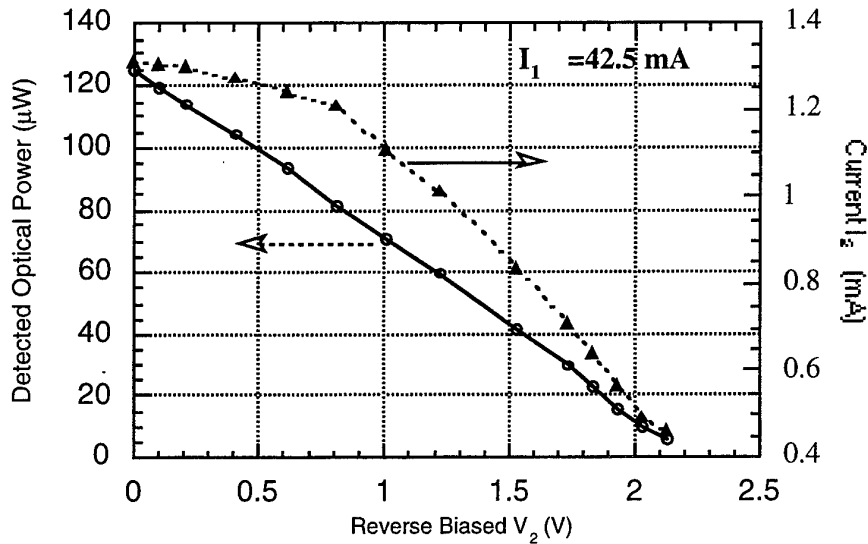


Fig.3.2 Output power variation while changing reverse bias on the tuning section for constant pumping current.

From the plot, it is seen that the leakage current from the tuning section also drops with bias, which is understood as the result of a decreasing in photo-generated current due to the reduced optical power. Several factors are responsible for the decrease of output power. First, due to the high carrier density in the gain section, increasing reverse bias in the tuning section enhances the lateral potential difference from gain to

tuning section, therefore enhancing lateral free carrier diffusion from gain to tuning section. This carrier leakage from the gain section decreases the net optical gain, therefore, reducing the stimulated radiation power. Second, the increasing in carrier density in the tuning section increases the free carrier absorption loss, resulting in decreased output power. The sharply decreasing power is a total result of both.

It is necessary to point out that the leakage current I_2 consists of a carrier diffusion portion from the gain section and the photo-generated current portion in the tuning section. The p-n junction reverse bias leakage current (p-n junction saturation current) is quite small, far less than $1\text{ }\mu\text{A}$ over our range of reverse bias, therefore it is eliminated from this analysis. The increase in carrier leakage from the gain section increases the diffusion current portion, but the decrease in output power decreases the photo-generated current portion. As seen from the plot, I_2 drops at first more slowly than the power drop. This is clear evidence that the diffusion leakage current portion is increasing as if we suppose photocurrent is the only source of leakage current, I_2 should linearly follow the decrease in power. The super-linear behaviour of I_2 in the plot can be used to estimate the diffusion current increase: at $V_2 = -0.8\text{V}$, diffusion current reaches its maximum, and the diffusion current increase from its value at $V_2 = 0\text{V}$ is $\sim 0.2\text{mA}$. As discussed in Chapter 1, this means $\sim 3 \times 10^{16}\text{ cm}^{-3}$ free carrier density increase in the region beneath the implanted region, and $\sim 4 \times 10^{12}\text{ cm}^{-3}$ carrier density increasing in the tuning section.

Another clear evidence of carrier diffusion in the device is the following experiment. When starting to pump the gain section from zero bias, the leakage current from the tuning section shows a sudden jump from its initial value, which is not proportional to the power output at all as shown in Fig.3.3 below. It is clearly that there is lateral carrier diffusion in the device after the flat band condition is achieved in the gain section.

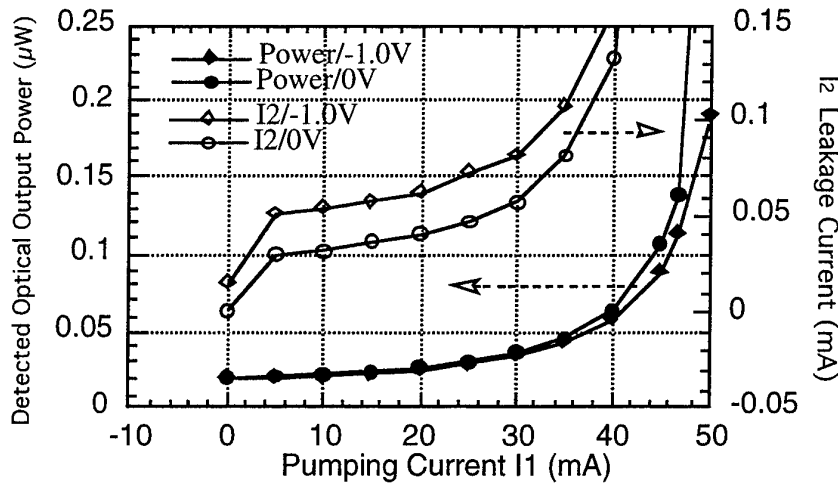


Fig.3.3 A zoom view of output power and leakage current when increasing the pumping current, for reverse bias 0 and 1 V, respectively.

Third, the photo-generated carrier effects on the power drop should be included. In the tuning section, the photo-generated minority electrons in the p-side and holes in the n-side overcome the potential barrier at the heterostructure interface by diffusion and drift across the active i-region to the opposite side under reverse bias, presenting a higher effective value of free carrier density in the active layer of the tuning section, resulting in a higher free carrier absorption loss in the cavity than that with no bias applied. This free carrier density or the absorption loss increases with increasing reverse bias since larger volume of photogenerated minority carrier being collected, resulting in decreased output power. As calculated in Chapter 1, the photocurrent effect produces the same order of magnitude free carrier density as the carrier diffusion effect in the tuning section.

An interesting experiment has been carried out to confirm the function of free carriers in this device. In this experiment, instead of a reverse bias, a forward bias is applied to the tuning section. Under constant pumping current on the gain section, the output power variation with applied forward bias to the tuning section is shown in Fig.3.4.

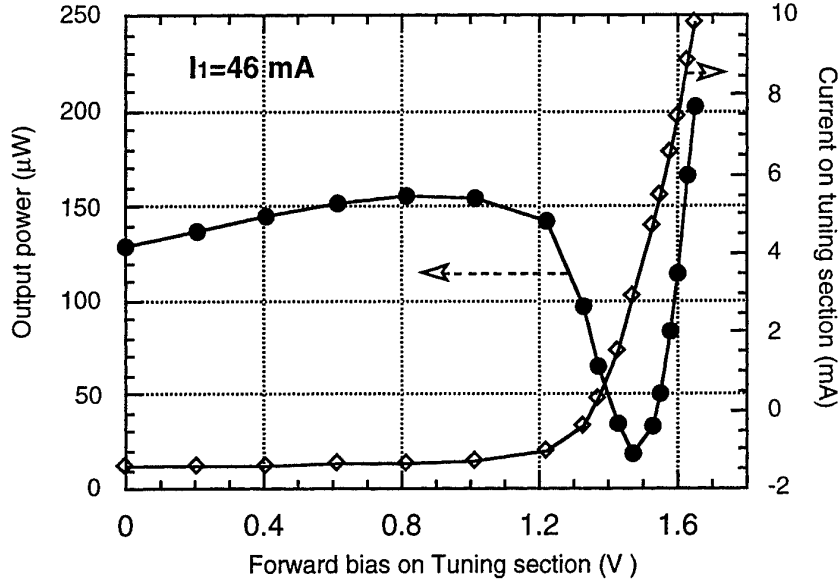


Fig.3.4 Tuning section forward biased characteristics. Output power and tuning section current variation with bias under constant pumping on the gain.

The result shows, in the initial stage, the output power increases first with the increase of applied forward bias, then decreasing to a minimum. Further increasing forward bias results in a sharp increase in output power. This is well understood now, since in the initial stage, forward bias draws the photo-generated minority carrier away from the active i-region of the tuning section, reducing the minority carrier amount being able to drift across the active i-region by diffusion in this tuning section, therefore, reducing the photo-generated free carrier density presented in the active layer of the tuning section and the free carrier absorption in the tuning section, just contrary to the reverse bias case. In the other hand, the carrier diffusion from gain section is reduced due to the forward bias decreases potential difference from gain to tuning section. Both effects results in the decrease of the photogenerated and diffused carrier density with the increase of applied forward bias, increases the output power of the device. Continue increasing forward bias starts the free carrier injection of the p-n junction in the tuning section, produces the decrease of the power due to free carrier absorption in this section. When the p-n junction flat band condition is reached in the tuning section, I_2 increases rapidly, resulting in a sharp increase of the free carrier density and decrease of the output power. Further increasing forward bias makes the tuning section toward to its threshold gain condition and start to contribute to the optical gain of the cavity, resulting a sharp increasing in output power. This is clear evidence that

the behaviour of photo-generated carrier and diffused carrier (from gain section) influences the device performance importantly.

A clear picture can be drawn from the analysis presented above: reverse bias on the tuning section changes the carrier densities of both sections and the carrier distribution along the whole cavity, varies the free carrier absorption loss in the tuning section and therefore, the output optical power. It is clear, even there is no lateral carrier diffusion from the gain section, the photo-generated carrier effect will still have important effect on the device performance. To eliminate this carrier diffusion and photo-generated carrier effects by ion implantation into the active layer in the isolation section and by band gap shifting therefore becomes very important in having a pure field effect device.

3.2.2. Tuning performance

Certainly, the electric field induced material absorption (rather than the free carrier absorption) variation in the tuning section also plays an important role in the device performance. The tuning of this device therefore is a combined result of field induced QCSE and carrier induced CIE.

Obviously, the free carrier absorption variations in the tuning section with reverse bias change the threshold condition as well as the gain spectrum. Tuning is also partly achieved by this effects. Accompanying the tuning, large variation in output power is associated. We therefore measured constant power output tuning and constant pumping current tuning, respectively.

Static tuning performance is evaluated by Fabry-Perot interferometer method. Fig.3.5 and Fig.3.6 show the results of constant pumping current and constant output optical power. As mentioned above, tuning is achieved partly because the gain spectrum variation with bias, and partly because of QCSE and CIE⁵ induced refractive index change. The tuning observed is a mixture result of all. The jumps in the plots correspond to the mode jumping. It is seen that a continuous tuning is obtained with only small reverse bias variation. A continue tuning range over 10GHz before mode jumping is achieved for constant current pumping, and over 60GHz continuous tuning (corresponding to the mode space of the device) before mode jumping is observed for constant optical power output. Complete tuning evaluation requires dynamic tuning

evaluation over a wide modulation frequency band (several GHz), therefore dynamic tuning evaluation is carried out.

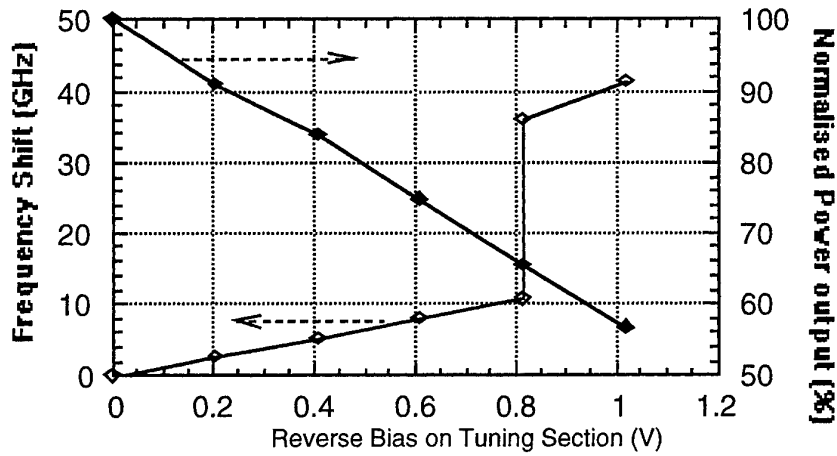


Fig. 3.5. Constant pumping current tuning. Pumping current is fixed at 52.7 mA.

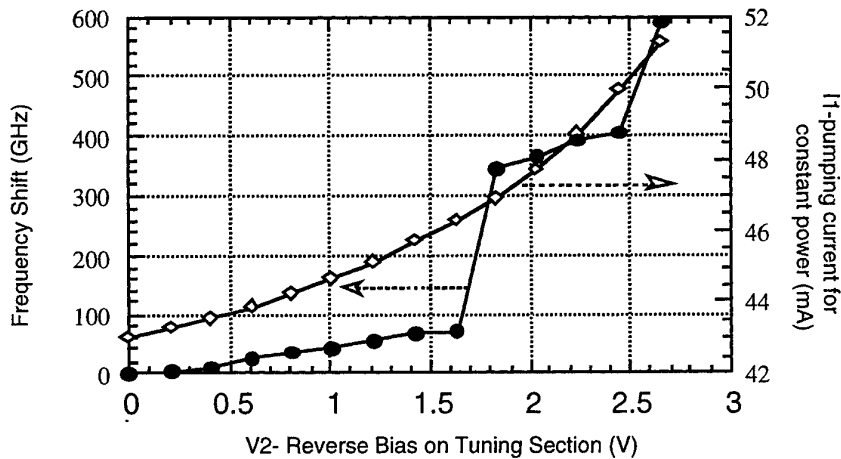


Fig. 3.6. Constant Power tuning performance. The power output is maintained at 3mW.

3.3. Dynamic tuning

As generally realised, CIE tuning is characterised in its frequency modulation (FM) response⁶. As in CIE tuning, due to its intrinsic carrier nature, thermal tuning mechanisms which are dominant at low modulation frequencies (<10 MHz) have the opposite sign from plasma and band gap narrowing tuning mechanisms which predominate at higher frequencies, leading to a non-uniform frequency modulation response⁶. By contrast field induced QCSE⁷ tuning is due to electric field induced

band gap narrowing which has no relation to carrier variation, and is a very fast tuning mechanism (in the picosecond region⁸), therefore, intrinsically its FM response is flat from DC up to very high (THz) modulation frequencies. The tuning due to carrier fluctuation induced gain spectrum shift is actually also a carrier effect, therefore, suffers from the same limitation as CIE. From the FM response measurement, it is therefore possible to identify QCSE tuning from the whole tuning response.

The FM response of the tunable laser can be measured from the optical spectrum of the modulated signal which is monitored with a high resolution Fabry-Perot interferometer. The lower frequency limit for such measurement is the resolution of the interferometer and the upper frequency limit is the maximum frequency deviation of the laser which maintains a measurable modulation index.

As the modulation may not be pure FM, an analysis needs to be carried out to separate the FM from the IM components.

The optical intensity of an intensity modulated signal can be written as

$$I = a^2[1 + \alpha \cos(\Omega t)] / \eta$$

where a is the amplitude of the electric field when no modulation is applied, α and Ω are the intensity modulation index and frequency, ω the carrier frequency (optical frequency), η is the impedance of the free space.

$$\sqrt{I} = a\sqrt{1 + \alpha \cos(\Omega t)} / \sqrt{\eta} \approx a[(1 - \frac{\alpha^2}{16}) + \frac{\alpha}{2} \cos(\Omega t) - \frac{\alpha^2}{16} \cos(2\Omega t)] / \sqrt{\eta}$$

when $\alpha \ll 1$

$$\sqrt{I} \approx a[1 + \frac{\alpha}{2} \cos(\Omega t)] / \sqrt{\eta}$$

therefore the electric field for a signal with both intensity and frequency modulation can be represented as

$$\begin{aligned} A &= a[1 + \frac{\alpha}{2} \cos(\Omega t + \theta)] e^{j[\omega t + \Delta \sin(\Omega t)]} \\ &= a \left\{ e^{j[\omega t + \Delta \sin(\Omega t)]} + \frac{\alpha}{4} e^{j[(\omega + \Omega)t + \Delta \sin(\Omega t) + \theta]} + \frac{\alpha}{4} e^{j[(\omega - \Omega)t + \Delta \sin(\Omega t) - \theta]} \right\} \\ &= a \left[e^{j\omega t} + \frac{\alpha}{4} e^{j[(\omega + \Omega)t + \theta]} + \frac{\alpha}{4} e^{j[(\omega - \Omega)t - \theta]} \right] e^{j\Delta \sin(\Omega t)} \end{aligned} \quad 3.1$$

where $\Delta = \Delta F / \Omega$ is the frequency modulation index, ΔF is the maximum frequency deviation, and θ the phase delay relative to intensity modulation.

Using the Bessel function property $e^{\frac{1}{2}z(t-1/t)} = \sum_{k=-\infty}^{\infty} t^k J_k(z)$ and setting $z = \Delta, t = e^{j\Omega t}$, we

replace $e^{j\Delta \sin(\Omega t)} = e^{\frac{\Delta}{2}(e^{j\Omega t} - e^{-j\Omega t})} = \sum_{k=-\infty}^{\infty} e^{jk\Omega t} J_k(\Delta)$ in Eq 3.1 and also

$$J_{k-1}(\Delta) + J_{k+1}(\Delta) = \frac{2k}{\Delta} J_k(\Delta) \text{ and } J_{k-1}(\Delta) - J_{k+1}(\Delta) = 2J'_k(\Delta)$$

yielding

$$A = a \sum_{k=-\infty}^{\infty} \left\{ \left[1 + \frac{k\alpha}{2\Delta} \cos(\theta) \right] J_k(\Delta) + j \frac{\alpha}{2} J'_k(\Delta) \sin(\theta) \right\} e^{j(\omega + k\Omega)t} \quad 3.2$$

or

$$A = a \sum_{k=-\infty}^{\infty} a_k e^{j(\omega + k\Omega)t} \quad 3.3$$

where

$$a_k = \left[1 + \frac{k\alpha}{2\Delta} \cos(\theta) \right] J_k(\Delta) + j \frac{\alpha}{2} J'_k(\Delta) \sin(\theta) \quad 3.4$$

The relative intensities at 0 and ± 1 orders (i.e. optical frequency ω and $\omega \pm \Omega$) can be written as

$$\frac{I_0}{a^2} = |a_0|^2 = J_0^2(\Delta) + \frac{\alpha^2}{4} J_0'^2(\Delta) \sin^2(\theta) \quad 3.5$$

$$\frac{I_1}{a^2} = |a_1|^2 = \left[1 + \frac{\alpha}{2\Delta} \cos(\theta) \right]^2 J_1^2(\Delta) + \frac{\alpha^2}{4} J_1'^2(\Delta) \sin^2(\theta) \quad 3.6$$

$$\frac{I_{-1}}{a^2} = |a_{-1}|^2 = \left[1 - \frac{\alpha}{2\Delta} \cos(\theta) \right]^2 J_1^2(\Delta) + \frac{\alpha^2}{4} J_1'^2(\Delta) \sin^2(\theta) \quad 3.7$$

Subtract Eq 3.6 and 3.7

$$\frac{I_1 - I_{-1}}{a^2} = \frac{2\alpha}{\Delta} J_1^2(\Delta) \cos(\theta) \quad 3.8$$

Using Eq 3.5 and 3.8 to replace $\frac{\alpha}{\Delta} \cos(\theta)$ and $\alpha^2 \sin^2(\theta)$ in Eq 3.6 we have

$$\frac{I_1}{a^2} = \left[1 + \frac{I_1 - I_{-1}}{4a^2 J_1^2(\Delta)} \right]^2 J_1^2(\Delta) + \left[\frac{I_0}{a^2} - J_0^2(\Delta) \right] \frac{J_1'^2(\Delta)}{J_0'^2(\Delta)} \quad 3.9$$

or, using $J'_0(\Delta) = -J_1(\Delta)$ and $J'_1(\Delta) = J_0(\Delta) - \frac{J_1(\Delta)}{\Delta}$ to transform Eq 3.9 gives

$$\frac{I_1 J_1^2(\Delta)}{a^2} = \left[J_1^2(\Delta) + \frac{I_1 - I_{-1}}{4a^2} \right]^2 + \left[\frac{I_0}{a^2} - J_0^2(\Delta) \right] \left[J_0(\Delta) - \frac{J_1(\Delta)}{\Delta} \right]^2 \quad 3.10$$

From Eq 3.10 the frequency modulation index Δ can be obtained and α and θ can then be found using Eq 3.5 and 3.8

$$\tan(\theta) = \frac{4aJ_1(\Delta)\sqrt{I_0 - a^2J_0(\Delta)}}{(I_1 - I_{-1})\Delta} \quad \text{and} \quad \alpha^2 = \frac{4I_0}{a^2J_1^2(\Delta)} - 4\frac{J_0^2(\Delta)}{J_1^2(\Delta)} + \frac{(I_1 - I_{-1})^2\Delta^2}{4a^4J_1^4(\Delta)}$$

In reality, the assumption of $\theta = 0$ has to be made based for three reasons:

- To use Eq 3.5, 3.8 and 3.10 to solve all three parameters, the carrier power for an unmodulated signal I_0 has to be used to normalise the modulated carrier and sideband power. The measurement of I_0 has to be carried out separately from the modulated measurements, introducing error due to drift..
- The dependence of θ with measured data is very weak, making the solution of Eq 3.8 uncertain when measurement errors exist.
- According to theoretical study on QCSE in MQW, the refractive index change is closely link to the absorption change by the Kramers-Kronig relation. In the time scale we are interested in, the delay between them is negligible.

Under the assumption $\theta = 0$, Eq 3.5, 3.6 and 3.7 can be simplified to

$$|a_0| = J_0(\Delta) \quad 3.11$$

$$|a_1| = \left(1 + \frac{\alpha}{2\Delta}\right) J_1(\Delta) \quad 3.12$$

$$|a_{-1}| = \left(1 - \frac{\alpha}{2\Delta}\right) J_1(\Delta) \quad 3.13$$

It is seen from (3.12) and (3.13), if $|a_1| \approx |a_{-1}|$, we have $\alpha \approx 0$, or there is no intensity modulation. This is the case of pure frequency modulation. In another case, if IM index is much smaller than the FM index and the FM index is not too large.

$$\Delta = \frac{|a_1| + |a_{-1}|}{|a_0|} = \frac{\sqrt{I_1} + \sqrt{I_{-1}}}{\sqrt{I_0}} \quad 3.14$$

$$\frac{\alpha}{2} = \frac{||a_1| - |a_{-1}||}{|a_0|} = \frac{|\sqrt{I_1} - \sqrt{I_{-1}}|}{\sqrt{I_0}} \quad 3.15$$

We can therefore obtain frequency and intensity modulation index by measuring zero and ± 1 order side band intensity. From $\Delta = \Delta F / \Omega$, we can have the maximum frequency deviation ΔF at modulation frequency Ω .

The measurement set-up is shown in Fig.3.8. The RF source has an output impedance of 50Ω . The tuning section of the laser is terminated by a 47Ω shunt resistance. Typical spectra recorded from digital oscilloscope are shown in Fig.3.8.

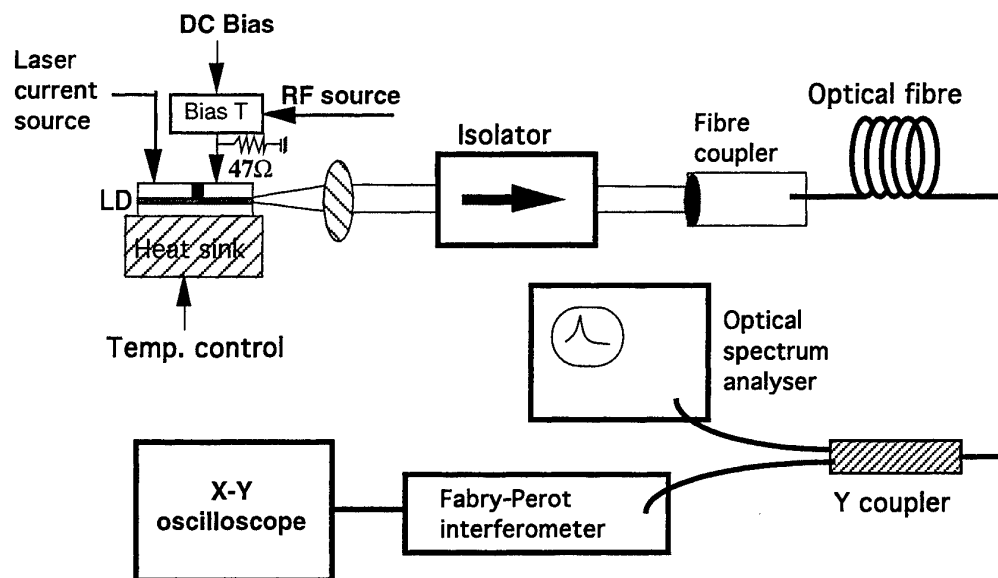


Fig.3.7 Set-up for dynamic tuning performance assessment of 2-section tunable laser.

As seen in Fig.3.8, the frequency deviation is measured from the Fabry-Perot interferometer in a different way corresponding to different frequency ranges. Above 100MHz, the side bands **a-e**, are used as deduced above; between 10kHz and 100 MHz, a large frequency deviation is produced with a low driving power, corresponding a large FM index Δ . Under this situation, twice the frequency deviation $2\Delta F$ is observed directly from the separation of two side band peaks⁶, as shown on **f**. Below 10kHz, where the modulation frequency lower than the scanning frequency of Fabry-Perot interferometer, the output show an instantaneous frequency shift as shown on **g**. The width of the multiple peaks is directly the frequency deviation. Fig.3.9 is the peak frequency deviation result in the modulation frequency range 5kHz~2GHz. It is seen for the modulation frequency below 500 MHz, the tuning response is quite uniform (less than 5 dB variation), tuning response drops very quickly, and a peak appears at about 1.18 GHz. The sharp decrease and the peak is identified as the result of parasitic parameters of this device, as described below.

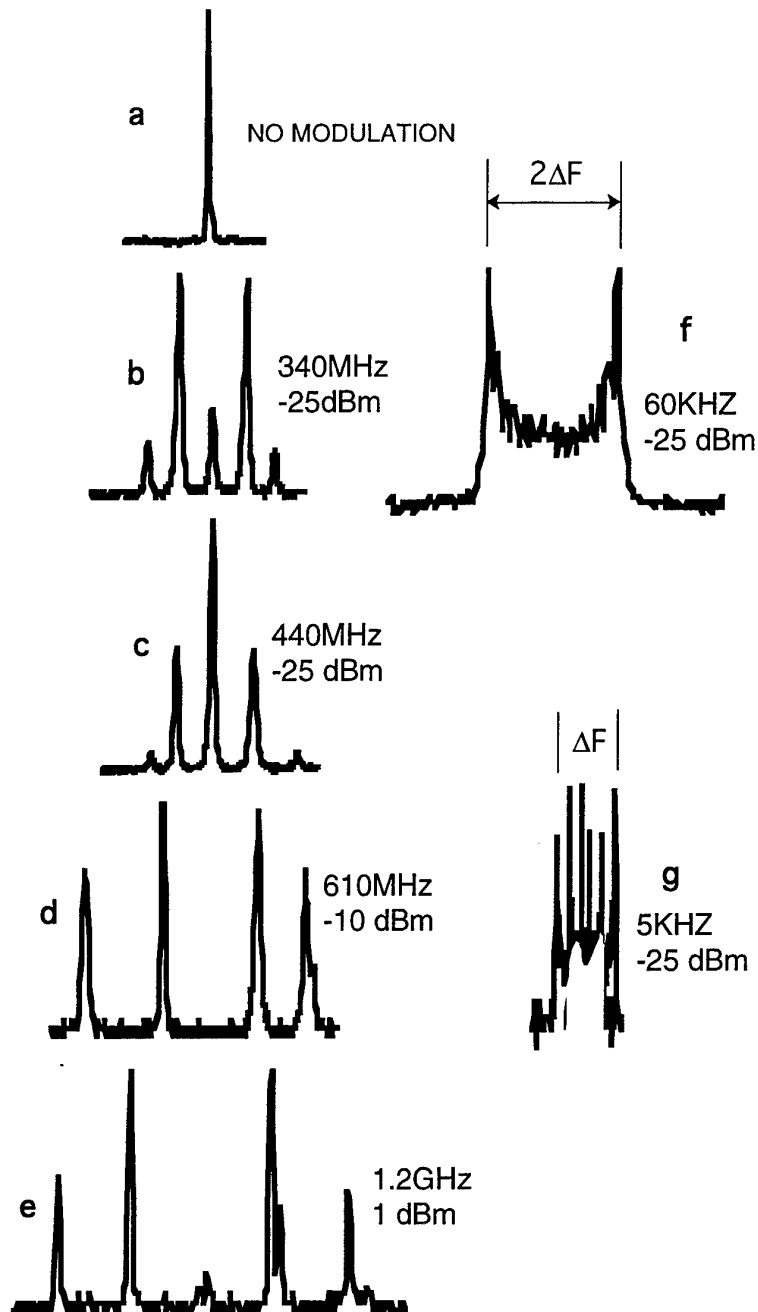


Fig.3.8 Fabry-Perot interferometer output spectra for measuring frequency deviation of a 2-section tunable laser. Modulation frequency and RF source power are quoted beside the spectrum.

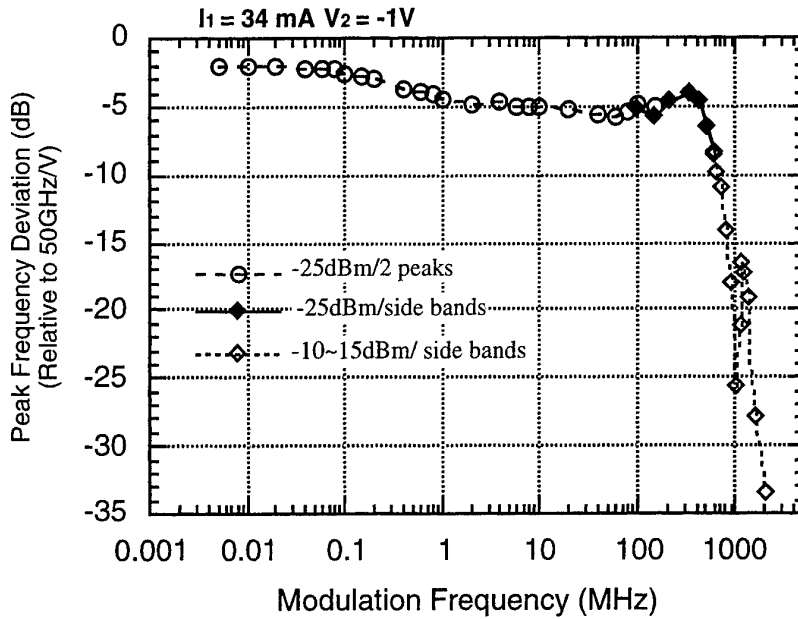


Fig.3.9. Peak frequency deviation (normalised to 50 GHz/V) variation with modulation frequency. Source power and measuring methods are given. Device is pumped at 34mA ($I_{th}=25 \text{ mA}$), with 1V reverse bias applied at tuning section.

The S11 reflection spectrum of the laser assemble is taken by using a network analyser. The result is shown on Fig.3.10. It is clear seen that a resonant peak appears at 1.1~1.2 GHz which is in coincident with the resonant peak observed in Fig.3.9.

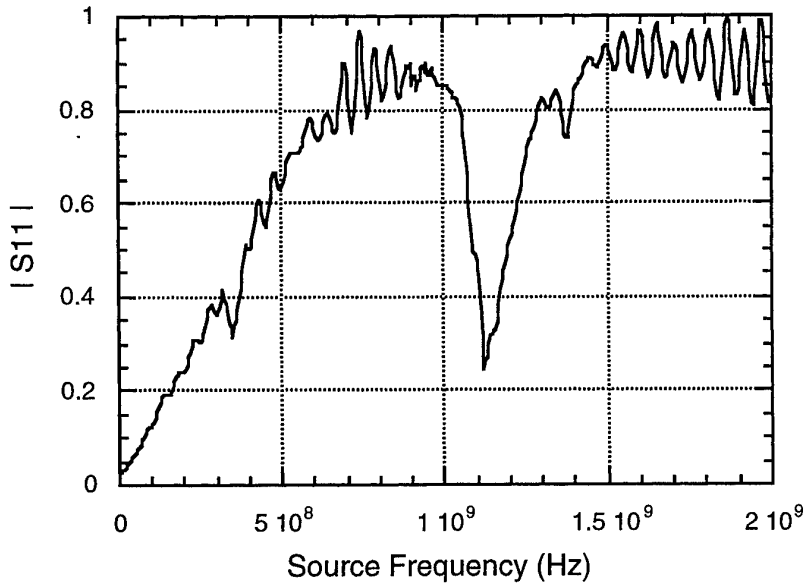


Fig.3.10. S11 reflection spectrum of the tunable laser assemble for dynamic characterisation. Source power is -10dBm.

A simple calculation suggests that this is due to the large device capacitance and the bonding wire inductance. By C-V method, we measured the capacitance of the tuning section of the test device. A 22pF capacitance is obtained under -1V bias. The bonding wire has a diameter of 25 μ m and a length of ~1mm, its inductance can be calculated by using

$$L=0.002 l [2.303 \log (4l/d)-1] \quad (\mu\text{H})$$

where l is wire length in cm, d the wire diameter in cm. We obtain $L=0.8$ nH for the bonding wire. The resonant frequency is therefore:

$$f_0 = \frac{1}{2\pi\sqrt{LC}} \cong 120 \text{ GHz}$$

which matches our experimental results very well. As we calculated in Chapter 2, this is mainly due to the large junction capacitance. To reduce this value by mesa etching and air bridge techniques is therefore necessary.

From Fig.3.9, it is observed within the low frequency range (<100MHz) there is no thermal effect observed due to the CIE tuning. It is therefore confident that at least within this frequency range, tuning is dominated by QCSE. Also for all devices we tested, no thermal effect was observed. The best result we obtained, as shown in Fig.3.11, has a very good response uniformity, within ± 1 dB over the frequency range 10kHz~100MHz. As a comparison, we also measured tuning by current injection on the same device, the result is shown Fig.3.12. It is quite clearly seen that the thermal effect induced by CIE tuning (5kHz~100kHz) cause a non-uniform response.

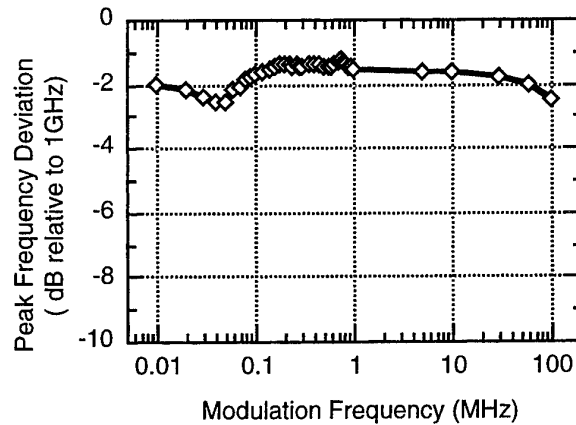


Fig.3.11. Tuning response of the 2-section tunable laser.
RF source power is -20dBm.

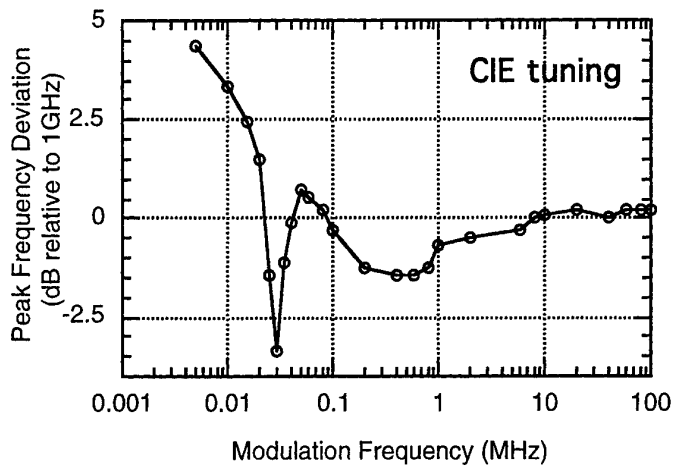


Fig.3.12. Tuning response by current injection in the same laser as Fig.3.11. RF source power is -20dBm.

In conclusion, static and dynamic tuning have been performed successfully. In static tuning, carrier diffusion and photocurrent are found to have important effects on device performance, but a large tuning range is obtained. In dynamic tuning, parasitic capacitance and inductance are found to limit device characterisation seriously, but no thermal effect is found, proving that the dominant tuning mechanism in the low modulation frequency range is QCSE.

References

1. Adamchuk_VK, Afanasev_VV and Akulov_AV, *Physica Status Solidi (A)*, **122** (1), p.347-354(1990)
2. Andreev_VM, Kalinovskii_VS, Larionov_VR, Rumyantsev_VD and Sulima_OV, "Injection-photon annealing of radiation induced defects during heterostructure concentrator solar cells operation", *Proceedings of the Intersociety Energy Conversion Engineering Conference*, 1989, **Vol.6**, pp.2823-2825
3. Hwang_RY, Lee_CP and Lei_TF, "GaAs/AlGaAs laser arrays with and without proton isolation", *Journal of the Chinese Institute of Engineers*, **12**(2), 255-61(1989)
4. Zavada_JM, Jenkinson_HA and Larson_DC, "Proton bombarded gallium arsenide: opto-electronic effects", *Proceedings of SPIE - The International Society for Optical Engineering*, 1986, **Vol.623**, pp.144-148

5. C. H. Henry, R. A. Logan and K. A. Bertness, *J. Appl. Phys.*, **52**, 4457-61(1981).
6. S.Kobayashi, Y.Yamamoto, M. Ito and T. Kimura, *IEEE J. Quantum Electron.*, **QE-18**, 583(1982)
7. D. A. B. Miller, D. S. Chemla, T. C. Damen, A. C. Gossard, W. Wiegmann, T. H. Wood and C. A. Burrus, *Phys. Rev., B*, **32**, 1043-60(1985).
8. A. M. Fox, D. A. B. Miller, G. Livescu, J. E. Cunningham, W. Y. Jan, *IEEE J. Quantum Electron.*, **27**(10), 2281-95(1991)

Chapter 4 Work in Progress and Future work

As discussed in Chapters 2 and 3, current diffusion from the gain section is quite important even if the ion implantation region reached the i-region where the waveguide core layer is laid. This is of course because of the lateral potential difference from gain to tuning section within the i-region. We are now considering an O^+ implantation scheme to penetrate through the whole i-region, therefore, changing the mobility of the carriers in the implanted region. This will block the carrier diffusion completely, as many researchers have demonstrated in planar stripe lasers. The problem remaining to be answered is how will such a region influence the laser if it is placed within the laser cavity. As there is no published report about this scheme, experiments are planned to optimise the dose, annealing condition and implantation energy in order to achieve lowest loss and highest isolation resistance.

In order further to reduce photocurrent effects and absorption loss, MQW band gap shifting is necessary. SrF_2 did not show good results after annealing, therefore, $SiO_2:P$ is chosen as the protecting dielectric film for IFVD. Experiments are in progress to use this new film and SiO_2 for achieving band gap shift.

Dynamic tuning results show that the modulation frequency range is seriously limited by the parasitic capacitance, therefore, a new design to cope with this problem is the best solution. The next generation of this laser will be grown epitaxially on SI GaAs. Devices will be processed into mesa structures, with the junction area only $20\text{ }\mu\text{m}$ in width and $300 \sim 600\text{ }\mu\text{m}$ in the cavity length. Air bridges will be used to connect the bonding pad and the top p-contact on the ridge. The whole device schematic diagram is shown in Fig.4.1 and Fig.4.2, and the main processing is:

1. MQW structure epitaxial growth on SI-GaAs substrate carried out by III-V Facility in Sheffield.
2. Dielectric film coating and lithography are performed first, then annealing at 900°C for 30 seconds to achieve MQW band gap shifting.
3. An ion implantation mask is prepared by lithography and etching, then O^+ implanting and annealing are performed to achieve best isolation while maintaining acceptable cavity loss.
4. p-Contact metal is deposited and patterned by photoresist lift-off, leaving $4\text{ }\mu\text{m}$ width contact metal.

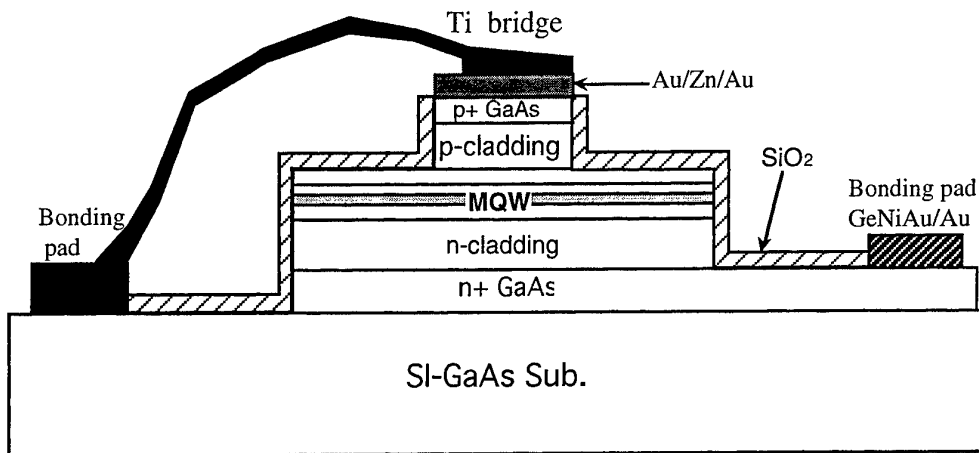


Fig. 4.1. The planned air bridged and mesa etched low parasitic two-section laser structure: cross view.

5. Ridge is defined by citric acid etchant and self-alignment etching where the metal functions as mask during etch and therefore no micro-scale alignment is required.
6. Lithography to form the etching window for mesa etching, and selectively etching the mesa down to n^+ -GaAs contact layer on one side of the ridge, and then another lithography and etching to etch the window down to SI-GaAs on the other side of the ridge.
7. PECVD is used to deposit SiO_2 on wafer, and then n-contact metal window is opened by lithography. Lift-off is used for patterning the metal.
8. Metallisation annealing at $\sim 400^\circ\text{C}$.
9. Coating with thick resist and opening window on SiO_2 for bridge contact, and depositing Ti; plating to thicken Ti to $\sim 2\mu\text{m}$. Lithography and HF etchant to pattern Ti into comb-shaped metal.
10. Thinning wafer down to $\sim 100\mu\text{m}$ and then clean wafer in solvent including acetone. The resist beneath comb-shaped Ti will be dissolved and the air bridge is formed.

Only step 6 and 9 are the extra steps when using SI-GaAs and air bridge technique, but both are not so difficult to perform. We are therefore confident of the success of this device. A new mask set design for processing this device is already in progress.

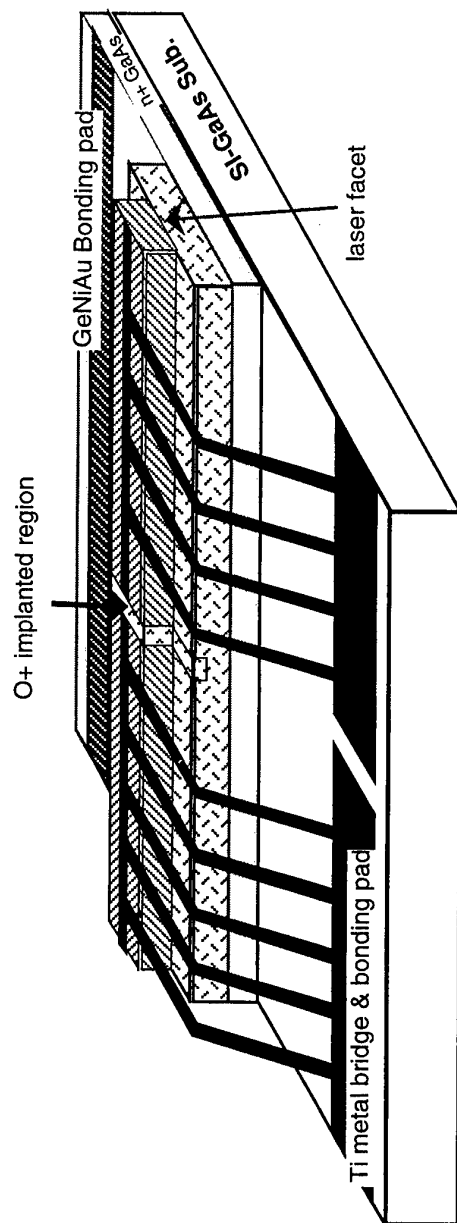


Fig.4.2. The planned air bridged and mesa etched low parasitic two section tunable laser : schematic whole structure view.

Chapter 5 Conclusion

During the second year of this programme we have successfully fabricated two-section QCSE tuned lasers, achieving continuous tuning ranges of over 60 GHz and FM response uniformity of $\pm 0.75\text{dB}$ over the range 10kHz to 100MHz and $\pm 2.5\text{dB}$ over the range 5kHz to 500MHz. Parasitic capacitance effects limit the response above this frequency.

We have also demonstrated the use of quantum well disordering by cap annealing for adjusting the relative operating wavelengths of gain and tuning sections, achieving a shift of 17 nm in their exciton peaks. Problems with laser fabrication from SrF_2 capped material have led us to alternative capping layers.

We have successfully fabricated both O^+ and H^+ isolated two section lasers and studied optimum isolation conditions.

In the next year of this programme we shall optimise the GaAs/AlGaAs laser structure and study tunable lasers based on QCSE in the InP/InGaAsP materials system.